eprints@whiterose.ac.uk
https://eprints.whiterose.ac.uk/

Mass segregation and sequential star formation in NGC 2264 revealed by *Herschel*[⋆]

T. Nony[1], J.-F. Robitaille[2], F. Motte[2], M. Gonzalez[2], I. Joncour[2], E. Moraux[2], A. Men'shchikov[3], P. Didelon[3], F. Louvet[3], A. S. M. Buckner[4], N. Schneider[5], S. L. Lumsden[6], S. Bontemps[7], Y. Pouteau[2], N. Cunningham[2], E. Fiorellino[8], R. Oudmaijer[6], P. André[3], and B. Thomasson[2]

[1] Instituto de Radioastronomía y Astrofísica, Universidad Nacional Autónoma de México, Apdo. Postal 3-72, 58089 Morelia, Michoacán, México e-mail: `t.nony@irya.unam.mx`
[2] Univ. Grenoble Alpes, CNRS, IPAG, 38000 Grenoble, France
[3] AIM, CEA, CNRS, Université Paris-Saclay, Université Paris Diderot, Sorbonne Paris Cité, 91191 Gif-sur-Yvette, France
[4] School of Physics and Astronomy, University of Exeter, Stocker Road, Exeter, EX4 4QL, UK
[5] Physikalisches Institut, Universität zu Köln, Zülpicher Str. 77, 50937 Köln, Germany
[6] School of Physics and Astronomy, University of Leeds, Leeds LS2 9JT, U.K.
[7] Laboratoire d'astrophysique de Bordeaux, Univ. Bordeaux, CNRS, B18N, allée Geoffroy Saint-Hilaire, 33615 Pessac, France
[8] INAF - Istituto di Astrofisica e Planetologia Spaziali (IAPS), via Fosso del Cavaliere 100, 00133 Roma, Italy

ABSTRACT

Context. The mass segregation of stellar clusters could be primordial rather than dynamical. Despite the abundance of studies of mass segregation for stellar clusters, those for stellar progenitors are still scarce, so the question on the origin and evolution of mass segregation is still open.
Aims. Our goal is to characterize the structure of the NGC 2264 molecular cloud and compare the populations of clumps and young stellar objects (YSOs) in this region whose rich YSO population has shown evidence of sequential star formation.
Methods. We separated the *Herschel* column density map of NGC 2264 in three subregions and compared their cloud power spectra using a multiscale segmentation technique. We extracted compact cloud fragments from the column density image, measured their basic properties, and studied their spatial and mass distributions.
Results. We identified in the whole NGC 2264 cloud a population of 256 clumps with typical sizes of ~0.1 pc and masses ranging from 0.08 $M_\odot$ to 53 $M_\odot$. Although clumps have been detected all over the cloud, the central subregion of NGC 2264 concentrates most of the massive, bound clumps. The local surface density and the mass segregation ratio indeed indicate a strong degree of mass segregation for the 15 most massive clumps, with a median Σ_6 three time that of the whole clumps population and $\Lambda_{MSR} \simeq 8$. We showed that this cluster of massive clumps is forming within a high-density cloud ridge, itself formed and probably still fed by the high concentration of gas observed on larger scales in the central subregion. The time sequence obtained from the combined study of the clump and YSO populations in NGC 2264 suggests that the star formation started in the northern subregion, that it is now actively developing at the center and will soon start in the southern subregion.
Conclusions. Taken together, the cloud structure and the clump and YSO populations in NGC 2264 argue for a dynamical scenario of star formation. Cloud could first undergo global collapse, driving most clumps to centrally concentrated ridges/hubs. After their main accretion phase, some, and probably the most massive, YSOs would stay clustered while others would be ejected from their birth sites. We propose that the mass segregation observed in some star clusters could be inherited from that of clumps, originating from the mass assembly phase of molecular clouds.

Key words. ISM: structure - stars: formation - methods: statistical - open clusters and associations: individual: NGC 2264

1. Introduction

Among the major open questions in the field of stellar cluster formation today is to define whether stellar properties, and especially their clustering characteristics and dynamical state, could be inherited from the properties of the clouds themselves. Mass segregation has been studied extensively in stellar clusters for decades, to investigate if the energy equipartition associated with two body relaxation (Spitzer 1969) causes high-mass stars to 'fall' toward the center of mass of clusters. As a matter of fact, mass segregation has been observed, as expected, in dynamically old globular and open clusters, but also in very young regions,

suggesting it was not due to dynamical evolution (see, e.g the review by Meylan 2000, and references therein). Primordial mass segregation prompts the question of whether there are preferential sites for high-mass star formation (Murray & Lin 1996) or whether the observed segregation is related to energy equipartition at all (e.g., Parker et al. 2016). Simulations indicate that primordial structure, if present, can be rapidly erased through dynamical interactions of the stars and expulsion of the gas (Parker & Meyer 2012; Fujii & Portegies Zwart 2016). Observational studies, however, show a weak, if any, correlation between the substructure and the age of the stellar clusters (Sánchez & Alfaro 2009; Dib et al. 2018). Hetem & Gregorio-Hetem (2019) indicate that stellar clusters did not significantly change in terms of structure within their first 10 Myrs, and corroborate the absence of correlation between mass segregation and the age of clusters,

---

as initially reported by Dib et al. (2018). Specifically, measuring the spatial distribution and mass segregation of molecular cloud fragments and comparing it to that of very young stellar objects is essential to study this link. A handful of studies have started investigating the mass segregation of molecular cores (Plunkett et al. 2018; Dib & Henning 2019; Román-Zúñiga et al. 2019), mostly focusing, first, on low-mass star-forming regions.

The *Herschel* observatory imaged, with an unprecedented sensitivity and angular resolution, the low- to high-mass star-forming clouds located at 100–500 pc and 0.7–3 kpc from the Sun (André et al. 2010; Motte et al. 2010). These surveys provide the opportunity to build large, if not complete, catalogs of cloud fragments with 0.01-0.1 pc (qualified of cores) to 0.1-1 pc sizes (called clumps). At these scales, clumps will likely fragment into cores, which could themselves be the direct progenitors of stars or small stellar systems. HOBYS[1], the *Herschel* imaging survey of OB young stellar objects (Motte et al. 2010), is the first systematic survey of a complete sample of nearby molecular cloud complexes forming high-mass stars. The wide-field photometric imaging, performed with both the SPIRE and PACS cameras of *Herschel*, aims at completing the census of high-mass star progenitors at 0.1 pc scales in essentially all the molecular cloud complexes at less than 3 kpc. The HOBYS sample contains seven massive, 3×10^5 to 3×10^6 $M_\odot$, molecular complexes at 1.4-3 kpc from the Sun, including Cygnus X and NGC 6334, and two intermediate-mass, a few 10^5 $M_\odot$, cloud complexes at 0.7-0.8 kpc, Vela C and Monoceros (Mon R1, Mon R2, NGC 2264).

HOBYS notably revealed a tight link between the density, dynamics, and clump population of the so-called ridges (Motte et al. 2018). The latter are high-density filaments ($n > 10^5$ cm^{-3} over ~5 pc^3) forming clusters of high-mass stars (e.g., Schneider et al. 2010; Hill et al. 2011; Nguyen Luong et al. 2011; Hennemann et al. 2012; Nguyen Luong et al. 2013; Tigé et al. 2017), whereas hubs are more spherical smaller structures forming at most a couple of high-mass stars (e.g., Schneider et al. 2012; Peretto et al. 2013; Rivera-Ingraham et al. 2013; Didelon et al. 2015; Rayner et al. 2017). The existence of ridges and hubs is predicted by dynamical models of cloud formation such as colliding flow or gravitationally-driven gas inflows simulations (e.g., Heitsch et al. 2008; Smith et al. 2009; Hartmann et al. 2012) and some analytical theories of filament collapse/conveyor belt (Myers 2009; Krumholz & McKee 2020).

The Monoceros OB1 (Mon OB1) cloud complex is located at a Gaia DR2 determined distance of 723^{+56}_{-49} pc (Cantat-Gaudin et al. 2018). In the mid-infrared, it displays a 2.5° (~30 pc) diameter half loop (Schwartz 1987), of which three 10 pc clouds have been imaged by *Herschel* as part of the HOBYS and Galactic Cold Cores key programs (Motte et al. 2010; Juvela et al. 2012). NGC 2264 and G202.3+2.5 lie at the eastern extremity of Mon OB1, Monoceros R1 is in the west. NGC 2264 is the best-studied cloud of the Mon OB1 complex (see the review by Dahm 2008). Over the past decade, a population of more than 1000 Young Stellar Objects (YSOs) at various evolutionary stages has been revealed (Teixeira et al. 2012; Povich et al. 2013; Rapson et al. 2014; Venuti et al. 2018). The NGC 2264 cloud is elongated in the NW-SE direction, with a gradient of star formation observed for YSOs from north to south (Sung & Bessell 2010; Venuti et al. 2018). NGC 2264 hosts the massive O7-type binary star S Monocerotis (S Mon), in the north, and the famous Cone Nebula, a triangular projection of molecular gas lying ~8 pc south of S Mon. The YSO population of NGC 2264 is mainly distributed in three sub-clusters: a cluster of pre-main

sequence stars in the north, in the vicinity of S Mon (Sung et al. 2009) and two clusters in the center. The central sub-clusters are often labeled according to their dominant objects, NGC 2264-IRS1, a B2-type star also known as Allen's source and -IRS2, a Class I protostar. IRS1 and IRS2 areas are also referred as NGC 2264-C and -D, or the Spokes cluster for NGC 2264-IRS2 region (Teixeira et al. 2006). These regions are still active sites of star formation, with many embedded Class 0/I protostars observed in millimeter continuum and lines (Williams & Garland 2002; Peretto et al. 2006; Young et al. 2006; Cunningham et al. 2016). Gas motions have also been reported from large scales, like the global collapse of NGC 2264-C (Williams & Garland 2002; Peretto et al. 2006), to small scales like protostellar outflows (Maury et al. 2009; Cunningham et al. 2016).

The paper is organized as follows. We introduce in Section 2 the *Herschel* column density map and clump catalog of the NGC 2264 cloud. In Section 3, we analyze the cloud structure using a multi-scale decomposition tool and divide the NGC 2264 cloud into three subregions. We then compare in Section 4 the physical properties of clumps in these subregions and discuss their spatial distribution and mass segregation. In Section 5, we compare the YSO and clump populations, in Section 6 we discuss mass segregation and propose a revised history for star formation in the NGC 2264 cloud. Finally, we summarize our conclusions in Section 7.

2. The NGC 2264 data set

2.1. Herschel *images, derived column density and temperature maps*

NGC 2264 was observed by the *Herschel* space observatory with the PACS (Poglitsch et al. 2010) and SPIRE (Griffin et al. 2010) instruments as part of the HOBYS (Motte et al. 2010) Key Program (OBSIDs: 1342205056 and 1342205057). Data were taken in five bands: 70 and 160 μm for PACS and 250, 350, and 500 μm for SPIRE with FWHM resolutions of 5.9″, 11.7″, 18.2″, 24.9″, and 36.3″, respectively. Observations were performed in parallel mode, using both instruments simultaneously, with a scanning speed of 20″s^{-1}. This results in a common PACS and SPIRE area of 1.0° × 1.2°, which corresponds to 10 pc × 13 pc at a distance of 723 pc.

Data were reduced using the *Herschel* Interactive Processing Environment (HIPE, Ott 2010) software, version 10.0.2751. SPIRE nominal and orthogonal maps were separately processed and subsequently combined and reduced for de-stripping, relative gains, and color correction with HIPE. PACS maps were reduced with HIPE up to Level 1 and, from there up to their final version (Level 3), using Scanamorphos v21.0 (Roussel 2013). The composite three-color (RGB = 250 μm/160 μm/70 μm) *Herschel* image of the NGC 2264 cloud is presented in Fig. 1.

High-resolution column density and temperature images, at the 18.2″ resolution of the 250 μm image, were built using the methods presented in Palmeirim et al. (2013) and Men'shchikov (in prep.). In short, we fitted pixel-by-pixel spectral energy distributions of the *Herschel* images with modified blackbody models to four, three, and two wavelengths (160/250/350/500 μm, 160/250/350 μm, and 160/250 μm) that were convolved to the lowest resolution of the images available in the three sets of wavebands. The higher-resolution information contained in the resulting density images, obtained with the smaller number of wavelengths, was transferred differentially to the 36″ resolution density image derived by fitting four wavebands, thereby increasing its resolution by a factor of two. We adopted a power

---

[1] see http://hobys-herschel.cea.fr
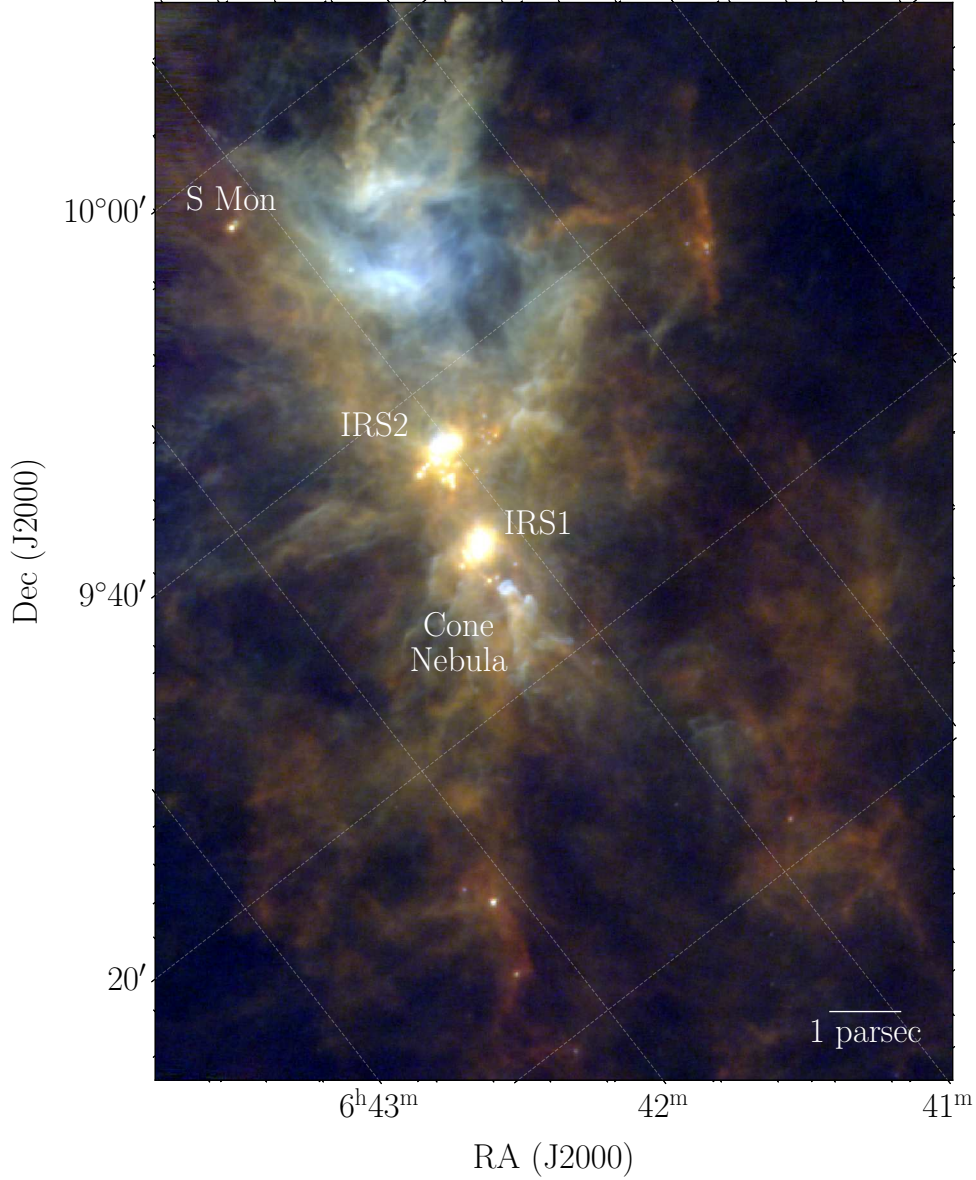
Fig. 1: Composite three-color *Herschel* image of NGC 2264: PACS 70 μm and 160 μm in blue and green, SPIRE 250 μm in red. The massive star S Mon, the central protoclusters NGC2264 IRS1 and IRS2 and the Cone Nebula are labeled. The blue component traces heated regions while earlier stage star-forming sites, such as clumps and filaments, are traced by the red component. The image has been rotated from the RA-Dec grid.

law approximation to the dust opacity law per unit of mass at submillimeter wavelengths, $\kappa_\nu = 0.1 \times (\lambda/300~\mu\text{m})^{-\beta}$ cm^2 g^{-1}, assuming a dust emissivity index $\beta = 2$ and a gas-to-dust ratio of 100. The resulting column density and dust temperature images are presented in Figs. 2 and A1. The column density map traces cloud structures from $\sim 2 \times 10^{21}$ cm^{-2} to 2.7×10^{23} cm^{-2}. The main cloud structure above $\sim 4 \times 10^{21}$ cm^{-2} displays a "Y" shape and consists of a hub of three filaments connecting toward a NW-SE ridge. The highest column densities, $N_{\text{H}_2} = 2-30 \times 10^{22}$ cm^{-2}, are reached at the center of NGC 2264, toward the two proto-stellar clusters NGC 2264-IRS1 and IRS2. Most of the low to medium (column) density gas has a dust temperature of ~ 14.5 K, decreasing down to 11-12 K within some high-density filaments and increasing up to 20-24 K toward IRS1 and IRS2. In the north, a large bubble of low density, heated gas, with 18-27 K over ~ 4 pc, is associated with a rosette-shaped nebula observed

in infrared and a couple of OB stars including the Herbig Ae/Be star called W90 (Dahm 2008).

Since Mon OB1 lies above the Galactic plane, the contamination of *Herschel* column density and temperature images by other clouds along the same line of sight is minimal (see Schneider et al. in prep. for a complete discussion of contamination effects). Absolute uncertainties on N_{H_2}, a factor of 2, and T_{dust}, a few degrees, depend mostly on the assumption taken for the dust mass opacity.

2.2. Clump catalog

Compact sources were extracted from the column density map at 18.2″ resolution (see Section 2.1) using *getsf* (v200124, Men'shchikov in prep.), a new multi-scale, multi-wavelength source and filament extraction algorithm based on the separation
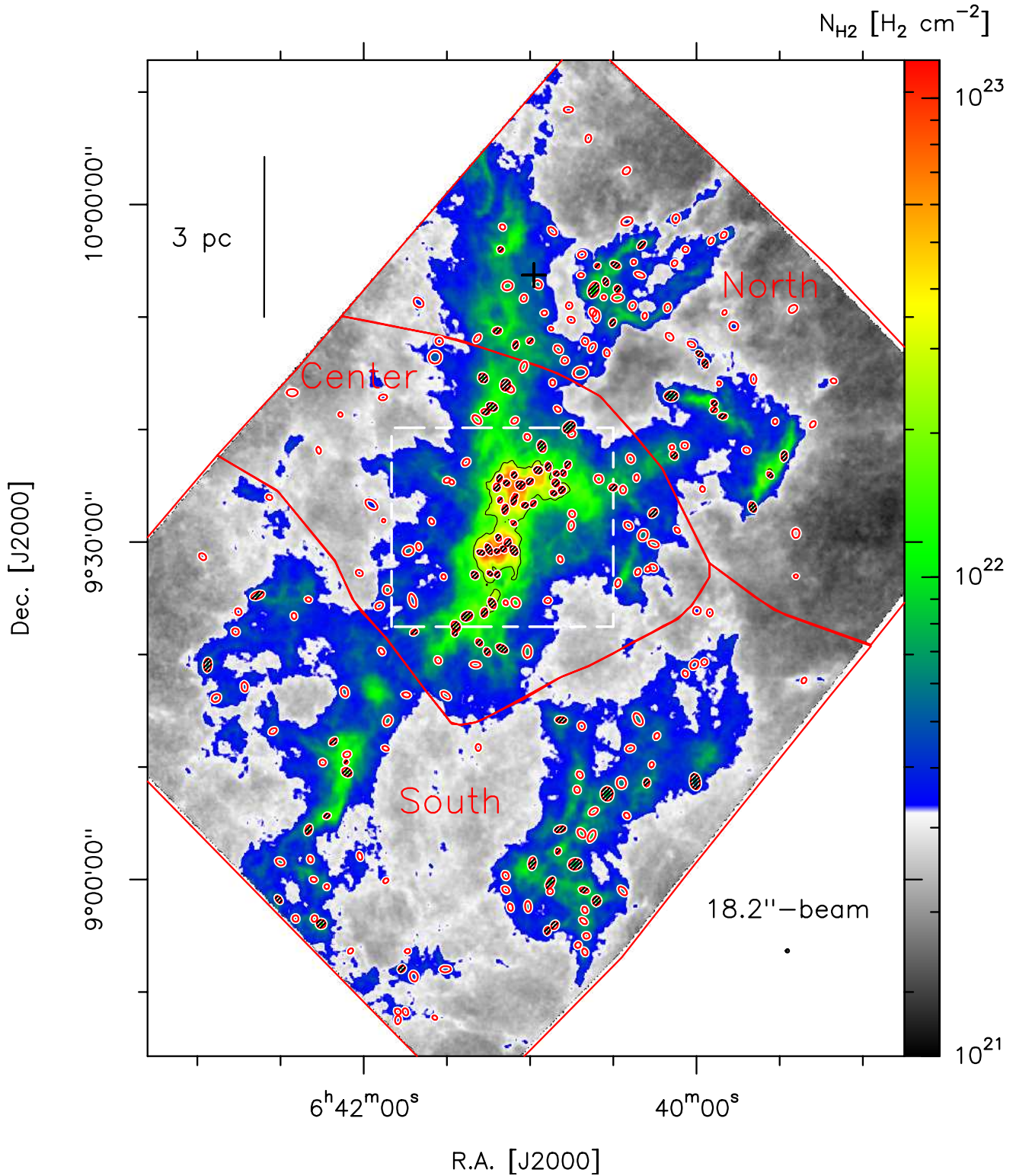
Fig. 2: The NGC 2264 cloud traced by its *Herschel* column density. The clumps extracted by *getsf* are indicated by ellipses, hatched for gravitationally bound clumps, empty otherwise. A contour at 2×10^{22} cm^{-2} is drawn to highlight the brightest parts. The resolution of the map, 18.2″, is shown in the lower-right corner and a scale bar is given in the upper-left corner. The outline and labels of the three subregions defined in Section 3.1 and used in the analysis are shown in red. The location of the zoom of Fig. 3 is shown with a white box.

of structural components. The method is a major improvement over its predecessors *getsources*, *getfilaments*, and *getimages* (Men'shchikov et al. 2012; Men'shchikov 2013, 2017). Original images are spatially decomposed into a set of 99 single-scale images, from two pixels to a maximum scale of 4 times the maximum size of sources of interest, 5.6″ to 232″ (or 0.8 pc) for the NGC 2264 HOBYS field. The decomposed images are processed and analyzed by *getsf* to separate three structural compo-
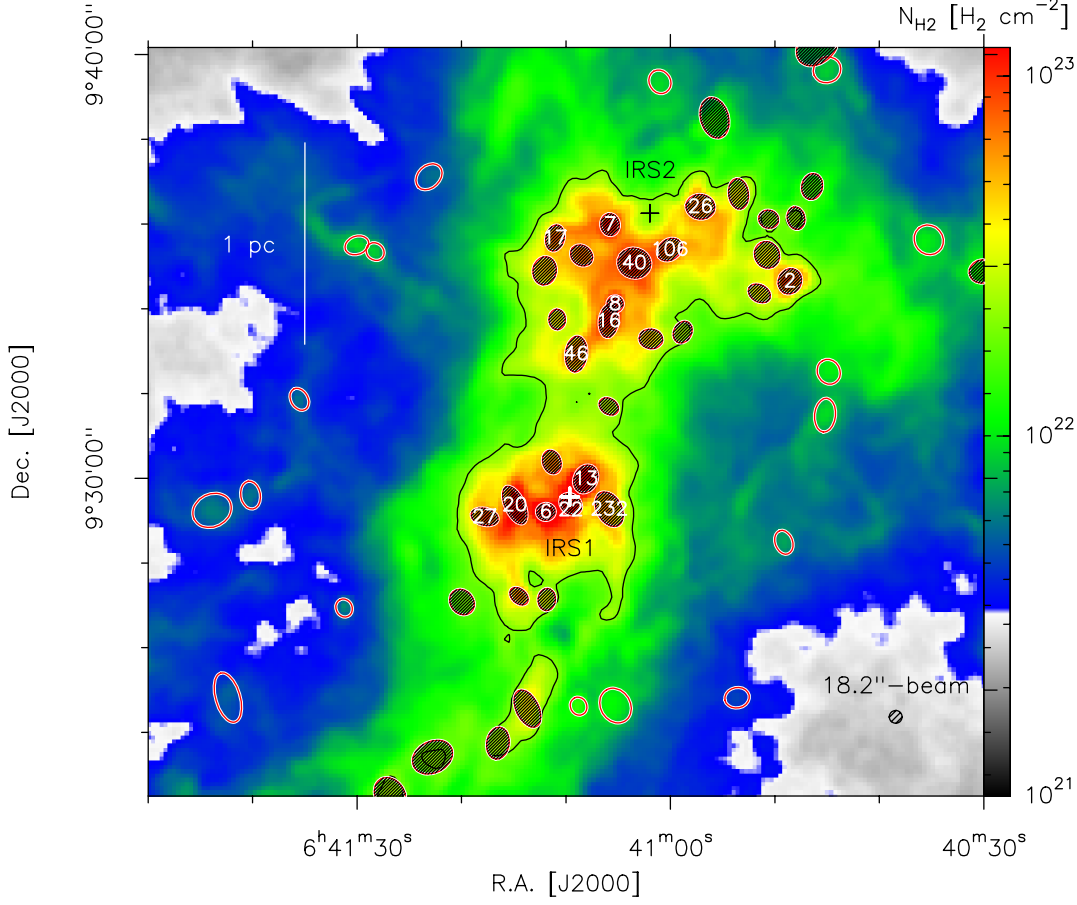
Fig. 3: Zoom toward the central part of NGC 2264, imaged through its *Herschel* column density. Same caption as Fig. 2. The white and black crosses show the location of the NGC2264 IRS1 and IRS2 sources, respectively. The associated IRS1 and IRS2 protoclusters contain most of the gravitationally bound clumps of this NGC 2264 subregion. The 15 most massive clumps ($M > 9.3 \, M_\odot$) are pinpointed with their number, the 16th is outside this zoom.

Table 1: Sample catalog of clumps identified in NGC 2264 using the *Herschel* column density map. The full table is shown in Table A1 and available in electronic form through CDS.

| #	R.A. [J2000]	Dec. [J2000]	$A \times B$ [$'' \times ''$]	PA [°]	Sig	$N_{H_2}^{peak}$ [$\times 10^{21}\, cm^{-2}$]	$N_{H_2}^{int}$ [$\times 10^{21}\, cm^{-2}$]	$FWHM_{dec}{}^a$ [pc]	T_{dust} [K]	M [$M_\odot$]	α_{BE}	$N_{H_2}^{back}$ [$\times 10^{21}\, cm^{-2}$]
1	100.5263	9.1742	18.2 × 18.2	18.3	80.5	18 ± 2	18 ± 2	0.03	20 ± 2	1.8 ± 0.2	0.3	11.5 ± 0.2
2	100.2023	9.5775	36.6 × 32.4	152.2	174.4	80 ± 6	286 ± 10	0.1	11.8 ± 0.3	30 ± 1	0.03	17.4 ± 0.6
3	100.2944	9.9336	27.4 × 26.2	24.5	104.8	19 ± 2	41 ± 2	0.07	15.7 ± 0.7	4.3 ± 0.2	0.21	8.8 ± 0.2
4	99.8894	9.5995	33.6 × 23.2	44.3	94.8	30 ± 3	68 ± 4	0.07	11.5 ± 0.4	7.0 ± 0.4	0.1	13.0 ± 0.3
5	100.2081	9.0423	30.1 × 23.4	168.7	76.2	11.2 ± 0.8	21.0 ± 0.9	0.07	12.3 ± 0.2	2.2 ± 0.1	0.31	6.5 ± 0.1
6	100.2997	9.4868	26.5 × 23.8	93.5	64.4	209 ± 12	400 ± 15	0.06	17.3 ± 0.7	41 ± 2	0.02	61 ± 1
7	100.2741	9.5998	31.3 × 26.3	7.2	56.5	82 ± 11	195 ± 14	0.08	15.0 ± 0.4	20 ± 1	0.05	46 ± 3
8	100.272	9.5686	22.8 × 22.8	22.6	47.7	77 ± 11	90 ± 13	0.05	15.4 ± 0.7	9 ± 1	0.07	52 ± 2
9	100.3104	9.4536	29.5 × 20.2	48.4	50.1	44 ± 8	77 ± 9	0.06	13.3 ± 0.4	8.0 ± 0.9	0.08	22.6 ± 0.6
10	100.5549	9.0945	31.8 × 22.5	115.5	42.3	11 ± 2	22 ± 3	0.07	12.6 ± 0.4	2.3 ± 0.3	0.31	9.7 ± 0.5
11	99.9603	9.6866	40.8 × 24.9	93.2	45.8	13 ± 1	35 ± 1	0.09	12.2 ± 0.2	3.6 ± 0.1	0.26	6.4 ± 0.2
12	99.9953	9.779	38.2 × 25.4	56.7	46.9	5.9 ± 0.2	17.0 ± 0.3	0.09	13.5 ± 0.3	1.7 ± 0.0	0.58	2.9 ± 0.0
13	100.2838	9.4998	41.0 × 32.3	153.3	48.6	138 ± 13	514 ± 21	0.11	16 ± 2	53 ± 2	0.03	41 ± 3
14	100.25	9.7985	31.9 × 27.8	129.0	40.5	5.9 ± 0.9	15 ± 1	0.08	15.1 ± 0.3	1.6 ± 0.1	0.65	7.1 ± 0.2
15	100.224	8.9245	38.6 × 28.0	174.2	44.6	5.3 ± 0.4	16.0 ± 0.6	0.1	13.0 ± 0.2	1.7 ± 0.1	0.61	3.9 ± 0.1
16	100.2746	9.5619	46.7 × 26.6	174.2	32.2	67 ± 11	204 ± 15	0.11	13.7 ± 0.7	21 ± 2	0.06	45 ± 3
17	100.2961	9.5946	37.4 × 25.9	166.2	31.2	46 ± 13	100 ± 13	0.09	14.0 ± 0.9	10 ± 1	0.1	35 ± 3
18	100.1488	9.9097	23.8 × 22.8	113.5	31.8	5 ± 1	9 ± 2	0.05	15.8 ± 0.4	0.9 ± 0.2	0.74	5.2 ± 0.3
19	100.1259	9.8254	37.1 × 24.9	155.3	39.4	6 ± 1	16 ± 2	0.09	16.5 ± 0.3	1.7 ± 0.2	0.69	5.9 ± 0.2
20	100.3121	9.4895	57.4 × 27.1	25.2	36.5	105 ± 13	382 ± 19	0.12	14.3 ± 0.4	40 ± 2	0.04	55 ± 3

^{a} source deconvolved size at FWHM, $FWHM_{dec} = (A \times B - 18.2^2)^{1/2}$, minimized at half the beam size

nents – sources, filaments, and background. The method flattens the sources and filament components to equalize their noise and background fluctuations, in order to reliably detect sources and filaments using intensity (here, column density) thresholds.

Detection of sources and filaments is done in the single-scale flattened images, whereas their measurements are done in the background-subtracted original image. The resulting catalog contains, for each extracted source, its peak and integrated column densities, $N_{H_2}^{peak}$ and $N_{H_2}^{int}$, with uncertainties, its major and minor axis sizes at FWHM, A and B, and the position angle of its elliptical footprint (PA). Also given is the source detection significance, S, which is a single-scale analog of the signal-to-noise ratio and the column density of the subtracted background, $N_{H_2}^{back}$. To measure the latter we averaged the background map provided by *getsf* over the source *FWHM*. A subset of this catalog is given in Table 1 and the complete table can be found in Table A1.

We also list in Table 1 the source FWHM sizes deconvolved from the beam, $FWHM_{dec}$, which provide an estimation of the physical sizes and range from 0.03 pc to 0.2 pc with a median value of 0.11 pc. The source average dust temperatures, T_{dust}, are listed with their associated uncertainties. They are defined as the mean and dispersion, respectively, measured over the source FWHM areas on the temperature map of Fig. A1. The measured temperature are averaged along the line of sight of each clump and generally overestimate by a few degrees the mean dust temperature of cold, shielded clumps (Hill et al. 2012). T_{dust} ranges from 11.5 K to 22.7 K with a median of 13.9 K. The temperature distribution in Fig. A4 show little variations, as 85% of the clumps have a temperature between 12 and 16 K.

A total of 256 sources has been extracted in NGC 2264 using *getsf*, they are plotted over the column density map in Figs. 2 and 3. The mass of the clumps is calculated from the integrated column density given by *getsf*, $N_{H_2}^{int}$ (see Table 1), following the equation:

$$
\begin{aligned}
M &= \mu_{H_2}\, m_H\, d^2\, \Omega_b\, N_{H_2}^{int} \\
&= 0.10\, M_\odot \left(\frac{\Theta_{HPBW}}{18.2''}\right)^2 \left(\frac{N_{H_2}^{int}}{10^{21}\,H_2\,cm^{-2}}\right),
\end{aligned}
\tag{1}
$$

with $\mu_{H_2} = 2.8$ the molecular weight per hydrogen molecule, m_H the hydrogen mass, $d = 723$ pc the distance to NGC 2264 and Ω_b the beam solid angle. Masses range from 0.08 $M_\odot$ to 53 $M_\odot$ with a median of 0.9 $M_\odot$. The relative uncertainty of clump masses is estimated to be less than 50% but the absolute uncertainty could be of a factor of 2.

2.3. YSO catalog

YSOs are selected from the 2MASS/*Spitzer* catalog established by Rapson et al. (2014) on the eastern part of the Mon OB1 molecular complex. The *Spitzer* map used by Rapson et al. (2014) covers most of the *Herschel* field, but small areas in the south, east and west, within which 10 clumps have been detected. Other YSO catalogs built over smaller areas (like one of, e.g., Kuhn et al. 2014) are not used here to keep the homogeneity of the YSO catalog. Rapson et al. (2014) use *Spitzer* IRAC (3.6-8μm) and MIPS 24μm data to select YSOs from their IR excess. They are thus sensitive to class 0/I sources while Cody et al. (2014) are not (since they use only IRAC data). Moreover, as opposed to Venuti et al. (2018) that present a spectroscopic study based on Gaia-ESO-Survey data, their spatial coverage is complete which is important for our study.

Among the 6381 YSOs within the field of view of the *Herschel* column density map, there are 87 Class 0/I protostars and 398 Class II pre-main sequence stars. Class III sources have been excluded from the studied sample because they are evolved YSOs, less relevant for comparison with the gas distribution. Besides, the Class III population in the catalog of Rapson et al. (2014) is significantly contaminated with field stars. The classification of YSOs was carried out by Rapson et al. (2014) using a color-based method developed by Gutermuth et al. (2009). Our sample also does not include the ∼20 intermediate- and high-mass sources that started forming a few 10^6 years ago, i.e. at the same time as the Class IIs of Rapson et al. (2014).

3. Analysis of the cloud structure in NGC 2264

Based on the YSO spatial distribution, the NGC 2264 star-forming region separates into two main subregions (Sung et al. 2008, 2009): the S Mon area and the region which encloses the two clusters associated with IRS1 and IRS2 (see Section 1). In line with these studies, the three-color, temperature and column-density *Herschel* images of Figs. 1-2 and A1 argue to separate the intermediate-column density, hotter northern subregion from the high-column density central subregion hosting the IRS1 and IRS2 protoclusters. The remaining part of the NGC 2264 cloud, which has intermediate column density and colder temperatures, is then labeled the southern subregion.

3.1. Splitting the NGC 2264 cloud into 3 subregions

In order to refine the outlines of the three NGC 2264 subregions, we performed a multiscale analysis of the NGC 2264 cloud. We used complex wavelet transforms described by Robitaille et al. (2014, 2019) to first calculate the power spectrum of the complete NGC 2264 region. While corresponding very well to the classic Fourier power spectrum, this method goes further by making it possible to visualize the spatial distribution of density fluctuations for any scale of the power spectrum. The decomposition is done with the directional and complex Morlet wavelet defined in the Fourier space as

$$
\begin{aligned}
\hat{\psi}(\boldsymbol{k}) &= e^{-|\boldsymbol{k}-\boldsymbol{k}_0|^2/2} \\
&= e^{-[(u-|\boldsymbol{k}_0|\cos\theta)^2 + (v-|\boldsymbol{k}_0|\sin\theta)^2]/2},
\end{aligned}
\tag{2}
$$

where $\boldsymbol{k} = [u, v]$ is the wavenumber, θ is the wavelet azimuthal direction and the constant $|\boldsymbol{k}_0|$ is set to $\pi\sqrt{2/\ln 2} \approx 5.336$ to ensure that the admissibility condition is almost met (Kirby 2005). From this decomposition, the amount of power for the density fluctuations as a function of spatial scales is calculated following the relation

$$
P^W(\ell) = \left\langle \left\langle |\tilde{f}(\ell, \boldsymbol{x}, \theta)|^2 \right\rangle_\theta \right\rangle_{\boldsymbol{x}},
\tag{3}
$$

where $\langle\rangle$ represents the averaging operation. The spatial scale ℓ is then converted to the Fourier wavenumber k following the relation $k = |\boldsymbol{k}_0|/\ell$.

Figure 4 shows the wavelet power spectrum of NGC 2264, corrected for the noise level and the 18.2″ beam. It can be fitted by a power law relation $P(k) = A\, k^\gamma$ (see fit parameters in Table 2), except for excess of power located at ∼ 0.15 arcmin^{-1} and ∼ 1.5 arcmin^{-1} corresponding respectively to scales of ∼ 1.4 pc and ∼ 0.1 pc. Figure 5 shows the spatial distribution of the power density fluctuations averaged over θ, $|\tilde{f}(\ell, \boldsymbol{x})|^2$, for these two scales as well as the 0.47 arcmin^{-1} (or 0.4 pc) scale located

Table 2: Global characteristics and cloud structure of NGC 2264 and its three subregions and fit values for the total wavelet power spectrum of NGC 2264 and for the Gaussian and coherent power spectra of the northern, southern and central regions.

Region name	Area [°²], [pc²]	$\overline{N_{H2}}$ [a] [×10²¹ cm⁻²]	N_{H2}^{back} [b] [cm⁻²]	$\overline{T_{dust}}$ [a] [K]	MnGSeg components	γ powerlaw	A [	P_0 ×10⁴² (H₂ cm⁻²)²	Noise]
NGC 2264	1.16, ~185	3.9	4.7	14.7	all	−2.3 ± 0.1	35 ± 7	−	(5.0 ± 0.5) × 10⁻³
Northern	0.38, ~61	2.9	4.0	15.4	Gaussian	−4.8 ± 0.1	0.06 ± 0.01	0.10 ± 0.02	(3.3 ± 0.5) × 10⁻³
					Coherent	−2.31 ± 0.09	9.0 ± 0.5	−	(3.3 ± 0.5) × 10⁻³
Central	0.26, ~41	6.6	7.3	14.9	Gaussian	−3.6 ± 0.1	0.08 ± 0.02	0.09 ± 0.02	(3.3 ± 0.5) × 10⁻³
					Coherent	−2.3 ± 0.1	299.0 ± 0.6	−	(3.3 ± 0.5) × 10⁻³
Southern	0.52, ~83	3.3	4.3	14.1	Gaussian	−4.02 ± 0.07	0.09 ± 0.01	0.13 ± 0.01	(3.3 ± 0.5) × 10⁻³
					Coherent	−2.43 ± 0.09	3.4 ± 0.5	−	(3.3 ± 0.5) × 10⁻³

[a] Typical column density and temperature, calculated as the average of the map in this area
[b] Typical background column density, calculated as the median background of clumps located in this area
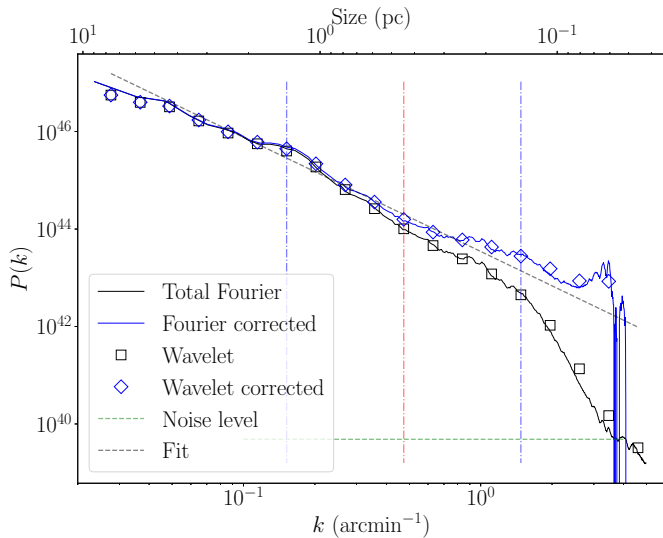

Fig. 4: The Fourier (solid lines) and wavelet (symbols) power spectra of the NGC 2264 region. Before fitting a $P(k) = A k^\gamma$ relation (dashed curve), the corrected power spectra are subtracted by the noise level (plateau at the end of the original power spectrum, green dotted horizontal line) and divided by the empirical SPIRE 250 μm beam. The power spectra present two bumps, located at 1.4 pc and 0.1 pc (vertical blue dot-dashed lines). The intermediate scale chosen to separate the three NGC 2264 subregions is indicated by a red dot-dashed vertical line.

between the two power excess. The first excess at 1.4 pc corresponds to the large-scale mass reservoir associated with the central part of the NGC 2264 cloud. It dominates in terms of density fluctuation at this spatial scale (see Fig. 5, Left panel) like do massive hubs or ridges in, e.g., the Cygnus X, Vela C, and NGC 6334 cloud complexes (Schneider et al. 2010; Hill et al. 2011; Tigé et al. 2017). This excess is also measured on NGC 2264 using the Δ-variance method (Schneider et al. in prep.). The 0.1 pc-scale image (see Fig. 5, Right panel) displays smaller scale structures, associated with clumps.

The intermediate scale of 0.4 pc, which separates the scales associated with the mass reservoir of the central ridge and the mass reservoir of small-scale clumps, was chosen to refine the division of the NGC 2264 cloud into three subregions. The outline of the northern, central, and southern subregions are set to go through saddle points (see Fig. 5, middle panel). The global characteristics of these subregions observed on the *Herschel* column density and temperature images are listed in Table 2.

3.2. Segmentation of the coherent and Gaussian components of the cloud structure

We applied the Multiscale non-Gaussian Segmentation (MnGSeg) technique in order to investigate the hierarchical properties of the cloud structure in the three subregions of NGC 2264. This technique allows to separate the random spatial density fluctuations of a cloud from the dense, coherent structures, usually associated with star formation activities. While we expect the Gaussian component of a cloud to only consist of evanescent structures of the interstellar medium, its coherent component contains cores, clumps, hubs, ridges and other filamentary structures which correspond to the gas mass reservoir of present star formation. The non-Gaussian segmentation is done on wavelet coefficients as a function of orientations θ and scales ℓ (see Robitaille et al. 2019 for more details on the technique). The amount of power for the density fluctuations as a function of spatial scales, $|\tilde{f}(\ell, \boldsymbol{x})|^2$, can be calculated according to the spatial coverage of areas of interest following the relation

$$P^W(l) = \frac{1}{N_{\mathbb{L}}} \sum_{\boldsymbol{x}} \left\langle \mathbb{L}(|\tilde{f}(\ell, \boldsymbol{x}, \theta)|) |\tilde{f}(\ell, \boldsymbol{x}, \theta)|^2 \right\rangle_\theta, \quad (4)$$

where

$$\mathbb{L}(|\tilde{f}_{l,\theta}(\boldsymbol{x})|) = \begin{cases} 1 & \text{if } \boldsymbol{x} \text{ is inside the area of interest} \\ 0 & \text{if } \boldsymbol{x} \text{ is outside the area of interest,} \end{cases} \quad (5)$$

and

$$N_{\mathbb{L}} = \sum_{\boldsymbol{x}} \mathbb{L}(|\tilde{f}_{l,\theta}(\boldsymbol{x})|). \quad (6)$$

Figure 6 presents the Gaussian (random) and coherent wavelet power spectra for the three subregions of NGC 2264 and Table 2 lists the parameters of their fitted relation $P(k) = A k^\gamma + P_0$ for the Gaussian component and $P(k) = A k^\gamma$ for the coherent part. For all subregions, the coherent component dominates in terms of power over the Gaussian components. Moreover, the central subregion presents a Gaussian component which resembles, in terms of both power level and power law index, those fitted for the northern and southern subregions. In contrast, the coherent component of the central subregion possesses a power level several hundred times higher than that of the northern and southern subregions. The coherent spectrum of the central subregion also displays more irregularities compared to the coherent spectra of the northern and southern parts (see Fig. 6b). We notably recover the two power excess observed in Fig. 4. As shown by Robitaille et al. (2019), the small-scale spectra flattening modelled by the variable P_0 for the Gaussian components only is associated to the cosmic infrared background signal.
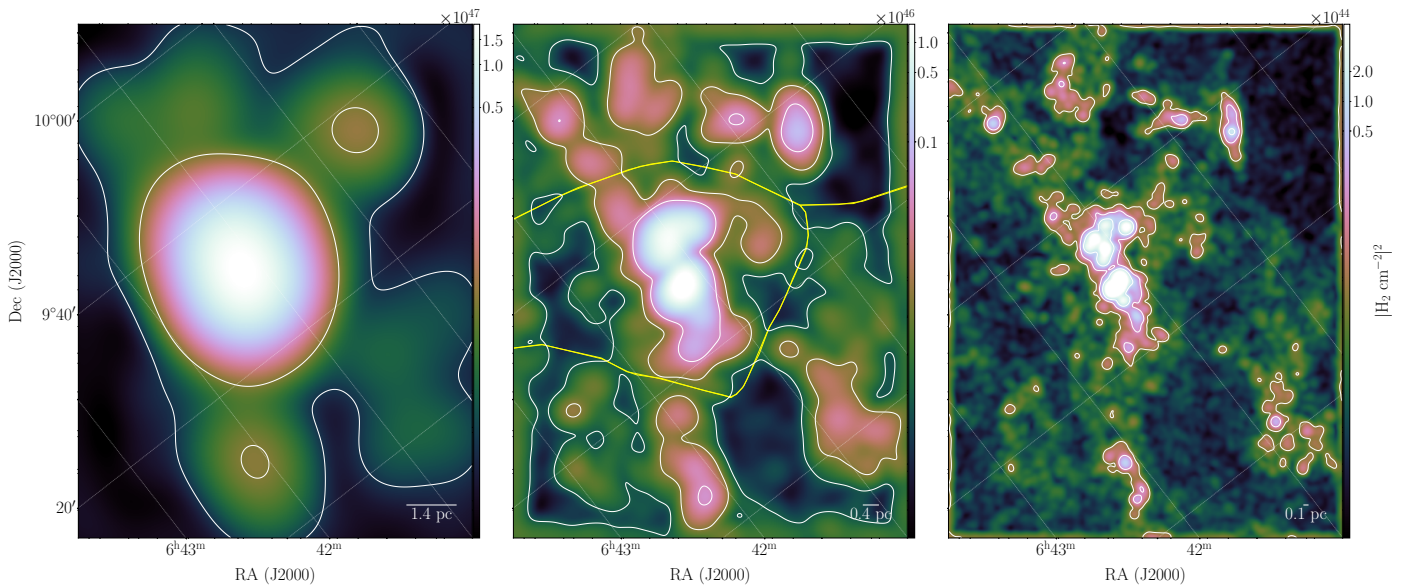
Fig. 5: Power density fluctuations of NGC 2264 measured by MnGSeg and averaged over θ for three scales: 0.15 arcmin^{-1} (or 1.4 pc, left panel), 0.47 arcmin^{-1} (or 0.4 pc, middle panel) and 1.5 arcmin^{-1} (or 0.1 pc, right panel). Images have been rotated from the RA-Dec grid (gray lines) to facilitate the wavelet decomposition. The yellow lines in the middle panel separate the three subregions of NGC 2264.
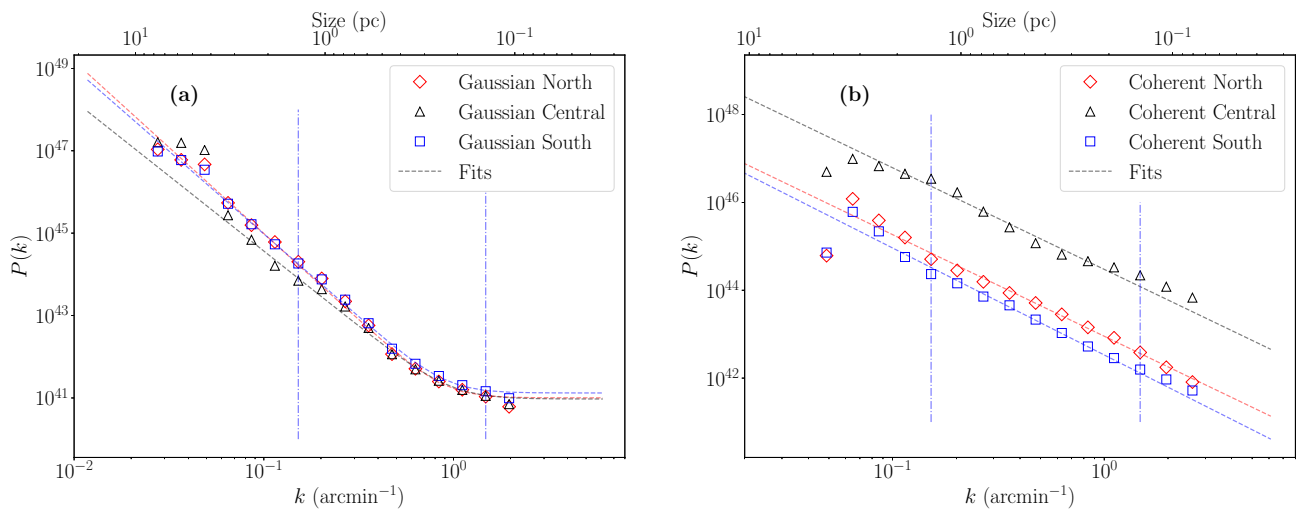
Fig. 6: The random Gaussian (in **a**) and coherent (in **b**) wavelet power spectra calculated by MnGseg for the three NGC 2264 subregions. The black and red dotted curve represents the fitted power law relations to the northern and central subregions. The coherent power spectrum of the central subregion stands out with ∼100 times more power and bumps located at 1.4 pc and 0.1 pc (vertical blue dashed lines).

Recently Robitaille et al. (2020) discussed and proved, using statistical models, that the non-Gaussian segmentation performed by MnGSeg can also be interpreted as the separation of a component of multifractal nature, the coherent part, from a monofractal component, the random Gaussian part. The multifractal nature of the coherent component means that its hierarchical structures are defined by a collection of power law indexes rather than by a single one, as it is the case for the monofractal geometry of the Gaussian component. These different fractal properties explain why the power spectra of the coherent components in Fig. 6b are more diverse and complex than those of the Gaussian components shown in Fig. 6a. It also suggests that the coherent component of a cloud (see Fig. 6b and Table 2) is the one that could reveal the complexity level of cloud structures,

which increases with the creation of large gravity potentials such as hubs and ridges. A more detailed analysis of the multifractal properties of the NGC 2264 cloud, its subregions, and clumps' local environment will be done by Robitaille et al. (in prep.).

4. Analysis of the population of clumps in NGC 2264

After estimating the completeness level of the catalogs of clumps identified in the three subregions of NGC 2264 (see Section 4.1), we characterize the main physical properties of clumps (see Section 4.2) and evaluate their boundedness (see Section 4.3). We then investigate the spatial distribution of clumps (see Section 4.4) and their mass segregation (see Section 4.5). Table 3

lists the main statistical parameters of the NGC 2264 cloud and its three subregions.

4.1. Completeness of the clump catalogs

To accurately compare the clump's properties between subregions, we estimated the completeness level and how it varies across the map. For this purpose, we injected a synthetic population of 1170 sources over the background image of NGC 2264, which is produced by getsf during the clump extraction process (see Section 2.2). Synthetic sources were split into 9 bins logarithmically spaced between 0.25 $M_\odot$ and 4.0 $M_\odot$, with a constant number of 130 sources per bin. Their chosen density profile is that of Bonnor-Ebert spheres with a central density increasing with the clump mass, in agreement with the profile observed for clumps. These synthetic clumps, once convolved by our 18.2″ angular resolution, display FWHM sizes of about 0.12 pc (or 35″) corresponding to the median size of extracted sources. We ran the extraction algorithm *getsf* on the synthetic image with the same parameters as for the observations. In total, 695 out of 1170 (59%) sources have been recovered.

Figures A2a-b show the detection rate of synthetic sources injected on the NGC 2264 background image. From the detection rate versus mass curve of Fig. A2a, we estimated a global 90% completeness level of ∼1.7 $M_\odot$. 74 (29%) clumps of Table 1 lie above this completeness level.

The completeness level of any source extraction procedure does however depend on the intensity of the source background. We therefore computed, for each identified sources, its contrast, defined as $C = N_{H_2}^{peak}/N_{H_2}^{back}$ and plot the detection rate against source contrast in Fig. A2b. A minimum contrast of 0.4 is required to detect a source, while all sources with $C > 1.7$ are detected. The 90% completeness level is reached for a source contrast of $C = 1.1$, that is for clumps with $N_{H_2}^{peak} = 1.1 \times N_{H_2}^{back}$. As shown in Fig. 2 and Tables 1 and 2, the background level varies strongly from the northern or southern subregions and central part of NGC 2264. We therefore used the median value of the clumps' background to characterize each subregion: $\overline{N_{H_2}^{back}} = 4 \times 10^{21}$, 4.3×10^{21} and 7.3×10^{21} cm^{-2} in the northern, southern and central subregions, respectively. Using the relation of mass versus peak column density found for both synthetic and observed clumps ($M \propto (N_{H2}^{peak})^{0.95}$, see Fig. A3a), we computed the associated mass threshold for clumps. We obtained a 90% completeness level of ∼1.5 $M_\odot$ for both the northern and southern subregions and a completeness level about two times larger, 2.7 $M_\odot$, for the central subregion of NGC 2264. As a consequence, some low mass clumps in the center may be overlooked by the extraction algorithm. The number of clumps with masses above these 90% completeness levels are 19, 22, and 33 in the northern, southern, and central subregions, respectively.

4.2. Main physical properties of clumps

The size and mass distributions of clumps in the northern, central and southern subregions are presented in Figs. 7a-b. As for the clumps sizes no significant variations have been observed between subregions (see Fig. 7a). The size distributions are all centered around a median value of ∼35″, corresponding to a deconvolved size of $FWHM_{dec} \sim 0.1$ pc at 723 pc. The three subregions also host a couple of clumps with *FWHM* sizes close to the beam, 18.2″, and 9 clumps with sizes larger than 57″ (or 0.2 pc). At a scale of ∼ pc, clumps will likely fragment into smaller and

denser cores, which could be the main mass reservoirs of individual protostars. Such cores have been observed in the two central protoclusters, IRS1 and IRS2 by Peretto et al. (2006) and Cunningham et al. (2016).

As for the mass distribution of clumps, it strongly varies between subregions (see Fig. 7b). While they are similar in the northern and southern subregions, the mass distribution in the central subregion is strongly shifted toward higher masses. Out of the 29 clumps with masses above 4 $M_\odot$, 24 are located in the central subregion.

4.3. Gravitational stability of clumps

In *Herschel* studies, the self-gravitating status of clumps is usually assessed using the Bonnor-Ebert ratio, $\alpha_{BE} = R_{dec}/R_{BE}$, where R_{dec} is the deconvolved clump radius (here $FWHM_{dec}$ and R_{BE} the radius of a critical Bonnor-Ebert sphere of the same mass, M, and temperature, T_{dust} as the source,

$$R_{BE} = \frac{M \mu_{H_2} m_H G}{2.4 \times k T_{dust}}, \tag{7}$$

where G and k are the gravitational and Boltzman constants. This parameter estimates the ratio between the thermal support and gravitational force and clumps with $\alpha_{BE} < 2$ are considered as gravitationally bound. The Bonnor-Ebert ratio should however be considered as a rough estimator of the gravitational boundedness of the clump, since it does not include the effects of turbulence, magnetic fields, or external pressure.

Although α_{BE} parameters theoretically depends on the mass, size, and temperature of the clump, the latter, which varies little within the sample (13.9^{+3}_{-1} K, see Fig. A4), has a small influence here. As illustrated by the mass versus size diagram shown in Fig. 8a, the separation between bound and unbound clumps appears close to horizontal in this logarithmic representation. This implies that a threshold on the Bonnor-Ebert parameter approximately corresponds to a threshold in mass, $\alpha_{BE} < 2 \Longleftrightarrow M \gtrsim 1$-2 $M_\odot$. This appears more clearly on the mass distributions shown in Fig. 8b. Bound clumps are significantly more massive than unbound clumps, with a median mass of 2.6 $M_\odot$ vs 0.5 $M_\odot$, respectively.

In the whole NGC 2264 cloud and following the Bonnor-Ebert criterium, 36% of the clumps are gravitationally bound. In more detail, half the clumps of the central subregion are bound while they are only ∼30% in the northern and southern subregions (see Table 3). This result is in line with the variation of column-density background in the central subregion when compared with the southern and northern subregions (see Table 2).

4.4. Spatial distribution of clumps

Despite the different completeness limits of the three NGC 2264 subregions (see Section 4.1), clumps appear homogeneously distributed: 74, 97, and 85 in the northern, central, and southern subregions, respectively (see Table 3), of which ∼30% lie above their 90% completeness limit. Note, however, that the density of clumps $\overline{\Sigma_{clump}}$, defined as the ratio between the number of clumps and the subregion area, is about twice in the central subregion that in the northern and southern subregions (see Table 3).

To further investigate the spatial distribution of clumps, we first applied nearest neighbor statistics, using the distance from the center of each clump to the peak position of its nearest neighbor. The resulting distributions of nearest-neighbor clump separation are plotted in Figure 9 for the three subregions of

Table 3: Distribution of clumps and YSOs in NGC 2264 and its subregions.

Region name	Clumps						YSOs		
	Total[a,b]	Bound[b,c]	Unbound[b,c]	$\overline{\Sigma_{\text{clump}}}$	Q^d	$\Lambda_{\text{MSR}}^{\text{med } d}$	Total[e]	Class 0/I	Class II
NGC 2264	256/100%	92/36%	164	~1.4 pc^{-2}	$\simeq 0.7$	7.8	485/100%	87	398
Northern	74/29%	21/28%	53	~1.2 pc^{-2}	$\simeq 0.8$	$\simeq 1$	156/32%	10	146
Central	97(96)/38%	48/50%	49(48)	~2.4 pc^{-2}	$\simeq 0.8$	3.7	302/62%	69	233
Southern	85(76)/33%	23(22)/27%	62(54)	~0.9 pc^{-2}	$\simeq 0.6$	$\simeq 1$	27/6%	8	19

[a] Number of clumps in each subregions and their corresponding fraction of the total population.
[b] The number of clumps in the area where YSOs have been detected is given in parentheses.
[c] Gravitationally bound clumps have a $\alpha_{\text{BE}} < 2$ parameter in Table 1. The fraction of bound clumps in the subregion population is indicated.
[d] The clustering Q parameter is calculated from Eq. (8). The median mass segregation ratio, $\Lambda_{\text{MSR}}^{\text{med}}$, measured for the $N_{\text{MST}} = 4$ to 15 most massive clumps, are estimated from Fig. 11.
[e] Total number of Class 0/I and Class II YSOs in each subregions and their corresponding fraction of the total population.
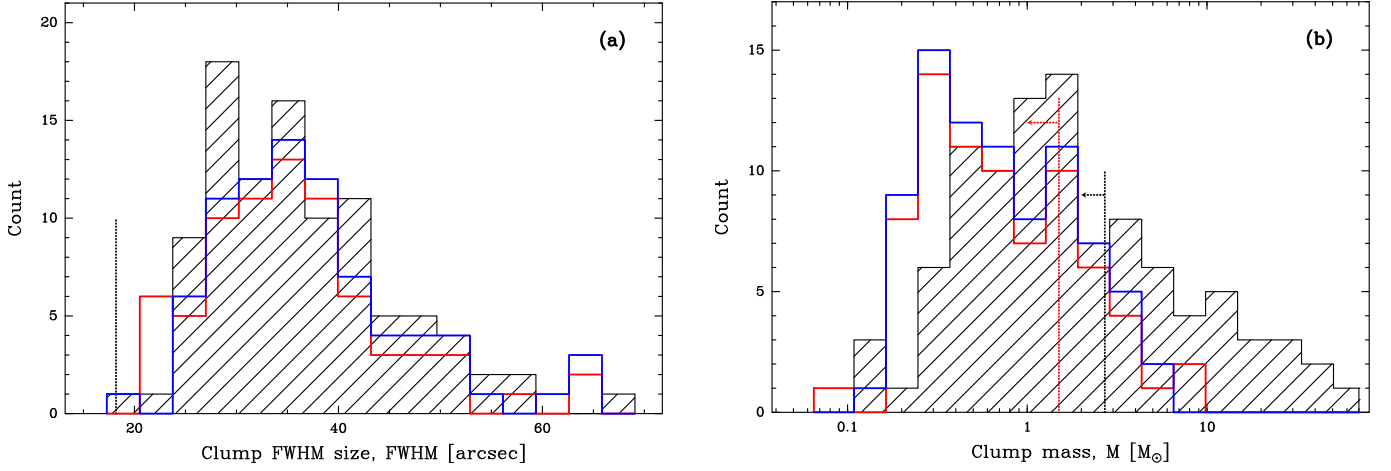
Fig. 7: Distribution of clump size (in **a**) and clump mass (in **b**) for the three subregions of NGC 2264: central (black hatched histograms), northern (red histograms), and southern (blue histograms) subregions. The central subregion has an excess of high-mass clumps compared the northern and southern subregions. The angular resolution of our observations, 18.2″, is given in **a**. The completeness levels, ~2.7$M_\odot$ in the central subregion and ~1.5$M_\odot$ in the northern and southern subregions, are indicated in **b** with dotted lines.
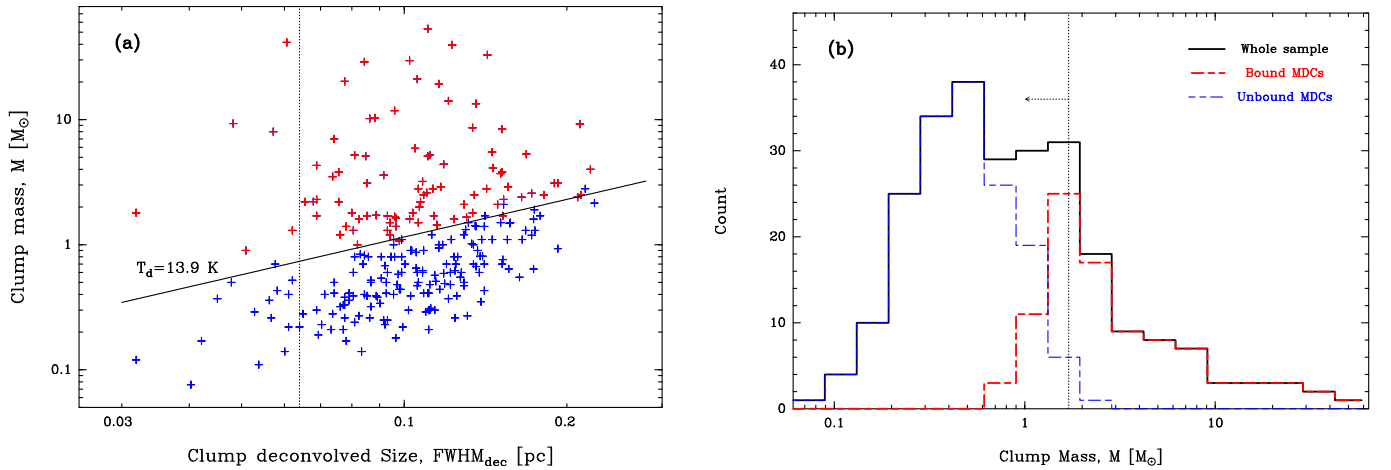
Fig. 8: Mass versus size diagram (in **a**) and mass distribution (in **b**) for the 256 clumps detected in the NGC 2264 cloud. Gravitationally bound and unbound clumps, with respectively $\alpha_{\text{BE}} < 2$ and $\alpha_{\text{BE}} \geq 2$, are located with red (resp. blue) markers (in **a**) and sum up in a red (resp. blue) histogram (in **b**). **a)** The critical Bonnor-Ebert sphere model ($\alpha_{\text{BE}} = 2$) at the median clump temperature, $T_{\text{dust}} = 13.9$ K, is plotted as a black solid line. The physical size of the beam at a distance of 723 pc is plotted as a vertical doted line. **b)** The global 90% completeness level is indicated with a doted line.
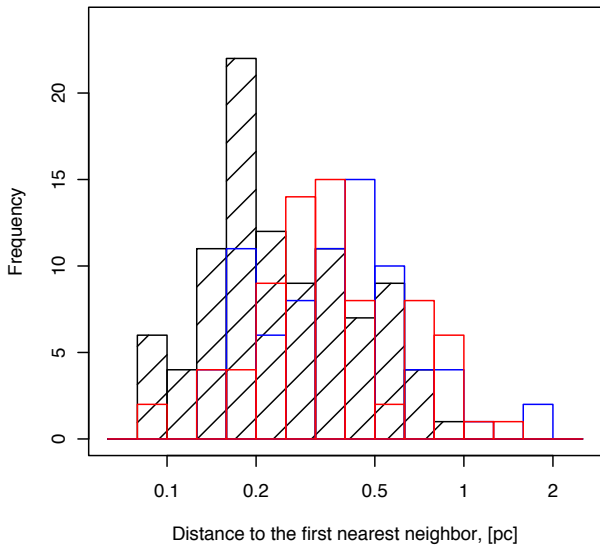
Fig. 9: Distribution of the distance to the first nearest neighbor for clumps in the central (black hatched histogram), northern (red histogram), and southern (blue histogram) subregions of NGC 2264. Clumps are 1.6 times more closely packed in the central subregion than in the two others.

NGC 2264. In the northern and southern subregions, clumps have similar median distances, 0.34 pc and 0.36 pc respectively, and cannot be statistically distinguished, according to a Kolmogorov-Smirnov (KS) test. The nearest neighbor distribution of the central subregion stands out with a large excess of clumps at short distance, ~0.1–0.2 pc, and a median clump separation of ~0.22 pc, which is 1.6 times smaller than in the northern and southern subregions. A KS test rejects, with a p-value below 10^{-4}, the hypothesis that the central and northern + southern subregions might have a common distance distribution. Interestingly, the clumps at the center of NGC 2264 are closely packed, with separations of about twice their median *FWHM* size, ~0.11 pc (see Section 4.2), and thus once their outer diameter. They are mostly located in the two IRS1 and IRS2 protoclusters of NGC 2264 (see Fig. 3).

We also computed the Q parameter (Cartwright & Whitworth 2004) for the NGC 2264 cloud and its three subregions (see Table 3). The Q parameter methods is based on the minimum spanning tree (MST), which is the set of straight lines (the edges) connecting a given set of points (here the clumps' center) without closed loops, such that the sum of all edges lengths is minimal. Q is defined as the ratio between the normalized mean edge length calculated by the MST, $\overline{l_{\mathrm{edge}}}$, and the mean clump separation, $\overline{s}$:

$$Q = \frac{\overline{l_{\mathrm{edge}}}}{\overline{s}}. \tag{8}$$

Q values above 0.8 are associated with centrally concentrated spatial distribution, while lower Q values indicate subclustering. With $Q \simeq 0.7$, the NGC 2264 cloud overall displays only a moderate amount of sub-clustering for its clump population. Locally, the southern subregion appears to be more subclustered compared to the central and northern subregions ($Q \simeq 0.6$ versus $Q \simeq 0.8$). On the column density map (see

Fig. 2), we indeed observed that its clumps are distributed either in a North-South filament joining the central subregion or in the south-western part of NGC 2264 .

4.5. Mass segregation of clumps

Mass segregation refers to a difference between the spatial distribution of massive objects compared to that of their lower-mass counterparts. The methods used to quantify mass segregation have evolved with our current view on the subject and are associated to slightly different definitions, but in general, they all compare the distribution of high- and low-mass stars. Amongst them, the local surface density Σ_j (Maschberger & Clarke 2011), and mass segregation ratio Λ_{MSR} (Allison et al. 2009), do not require the specific definition of a cluster center and are the most widely used. They most probably also give the most robust results when combined (e.g., Parker & Goodwin 2015). We applied both methods to measure the mass segregation of clumps in NGC 2264 and its subregions, using again the clumps peak position as a reference. The impact of the clumps spatial extent in these statistics will be investigated in future studies (Thomasson et al. in prep.).

The first method calculates the local surface density of source, Σ_j, within an area encompassing the jth nearest neighbor, at a distance of r_j:

$$\Sigma_j = \frac{j-1}{\pi r_j^2}. \tag{9}$$

As proposed by Maschberger & Clarke (2011), we took $j = 6$, as it constitutes a good compromise between estimating the local density and reducing low-numbers fluctuations (see also Casertano & Hut 1985).

Figures 10a-b present the Σ_6 versus M diagrams that investigate if high-mass clumps are in denser groups than their lower-mass counterparts. Since the clump populations of the northern and southern subregions exhibited similar behaviors in Sections 4.2–4.4., we assembled their clump samples. In contrast, we kept the central subregion alone since its clump sample had rather different characteristics. In the central subregion, the local surface density correlates with the mass of the clumps, with a Pearson correlation coefficient of 0.75 (see Fig. 10a). However, when accounting for the 90% completeness level of 2.7 $M_\odot$ (see Section 4.1), one can not exclude low-mass clumps in high-density groups have not been detected. Therefore, the most robust result of this Σ_6 analysis is that high-mass clumps in the central subregions are only found in high-density groups. The 15 most massive, >9.3 $M_\odot$, clumps in NGC 2264, closely packed in the IRS1 and IRS2 protoclusters (see Fig. 3 and Section 4.4), have a median Σ_6 density about three times that of all clumps in NGC 2264 center. Conversely, the lower-mass clumps in the northern and southern subregions do not present a privileged location in high- or low-density groups according to their mass (see Fig. 10b).

The second method to quantify mass segregation compares the MST of the most massive objects (here clumps) of a sample with the MST of randoms subsets of objects in this sample (see Allison et al. 2009). The mass segregation ratio, Λ_{MSR}, is calculated as

$$\Lambda_{\mathrm{MSR}}(N_{\mathrm{MST}}) = \frac{\overline{l_{\mathrm{random}}}}{l_{\mathrm{massive}}} + \frac{\sigma_{\mathrm{random}}}{l_{\mathrm{massive}}}, \tag{10}$$
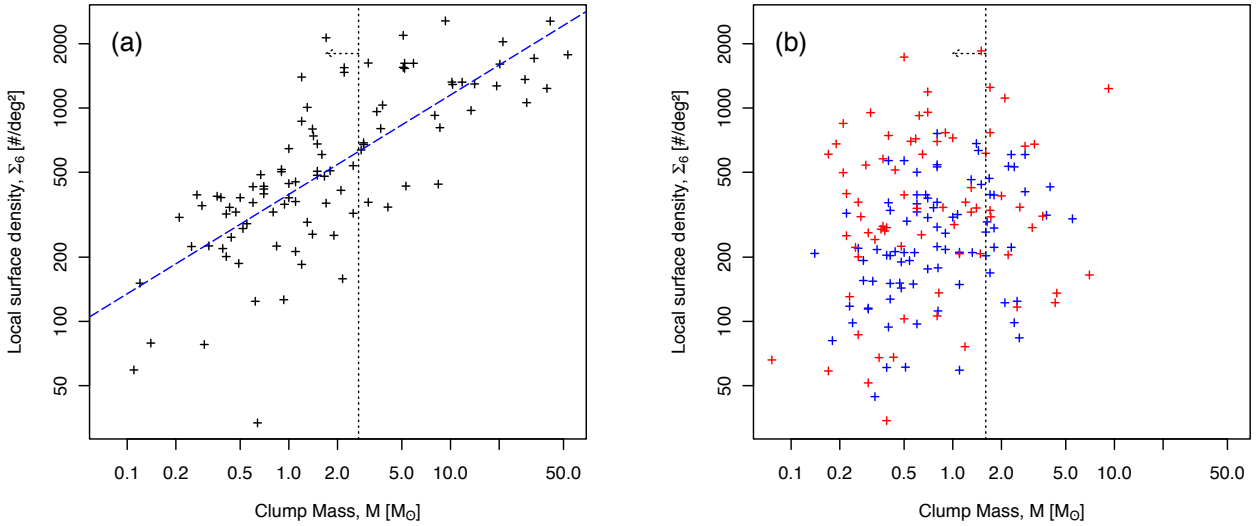
Fig. 10: Local surface density Σ_6 as a function of the mass of the clump for the central subregion of NGC 2264 (in **a**, black markers) and in the northern and southern subregions (in **b**, red and blue markers, respectively). The potential correlation between Σ_6 and M in **a**, $\Sigma_6 \propto M^{0.47}$, is represented by a dashed blue line, in both **a** and **b**. Completeness levels are indicated by vertical dotted lines.
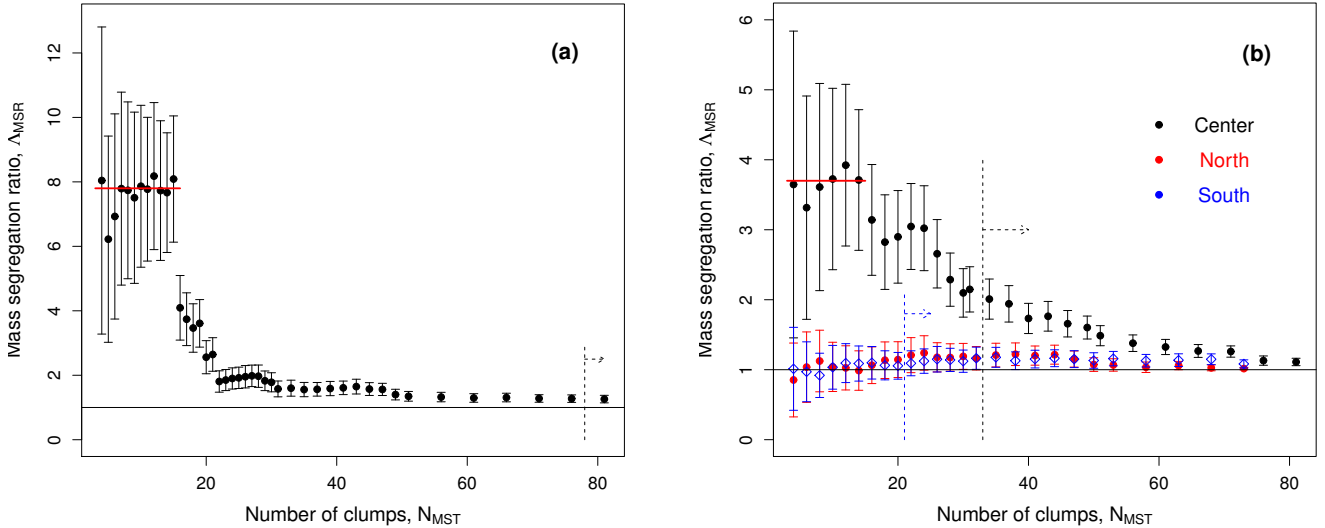
Fig. 11: Mass segregation ratio, Λ_{MSR}, as a function of the numbers of clumps, N_{MST}, in the NGC 2264 cloud (in **a**) and in its three subregions (in **b**). Error bars represent the $\pm 2\sigma$ uncertainties. Values above $\Lambda_{MSR} \simeq 1$ (black solid line) suggest mass segregation. Completeness levels are indicated with vertical dashed lines. **a)** The median segregation ratio for the 15 most massive clumps of NGC 2264, calculated over $N_{MST} = 4$ to 15, is $\Lambda_{MSR}^{med} = 7.8$ (red segment). **b)** The Λ_{MSR} function of clumps in the central subregion (black symbols) is three to two times larger than the one in the northern and southern subregions (in red and blue, respectively), over the range of $N_{MST} = 4 - 33$.

where $l_{massive}$ is the length of MST for the N_{MST} most massive clumps and $\overline{l_{random}}$ is the average length of MST for N_{MST} random clumps. It was computed for 500 sets of N_{MST} random clumps along with the associated standard deviation, σ_{random}. A value of $\Lambda_{MSR} \approx 1$ indicates that the spatial distribution of massive clumps is comparable to that of other clumps and therefore that there is no mass segregation. Larger Λ_{MSR} values suggest that massive clumps are more concentrated than their lower-mass counterparts.

Figures 11a-b display Λ_{MSR}, for an increasing number, N_{MST}, of the most massive clumps for the NGC 2264 cloud and its subregions. The clump population of NGC2264 appears to be strongly mass segregated, with values of Λ_{MSR} around 7.8 for

$N_{MST} \leq 15$. If we consider only the central subregion, which contains the most massive clumps, segregation is still present, but the Λ_{MSR} values decreases to ~ 3.7. This decrease is explained by smaller l_{random} values for clumps distributed in the central subregion than over the whole NGC 2264 cloud. In Fig. 11a, Λ_{MSR} drops to 4 for $N_{MST} = 16$, due to the fact that the 16th most massive clump is the first one located outside the IRS1 and IRS2 protoclusters. Mass segregation remain significant, with Λ_{MSR} values above 1 with more than 2 sigma uncertainty, up to $N_{MST} \simeq 30$. In contrast, for the clump samples of the northern and southern subregions, Fig. 11b do not reveal any mass segregation. The Λ_{MSR} plateau observed are listed in Table 3.

5. Combined analysis of the YSO and clump populations in NGC 2264

In this section, we analyze the YSO content of the NGC 2264 subregions (Section 5.1) and quantify the link between the YSO and clump populations (Section 5.2).

5.1. Distribution in the NGC 2264 subregions

The spatial distribution of the clump and YSO populations is illustrated in Fig. 12. The clump population is rather homogeneously distributed over the whole *Herschel* area (see Section 4.4) even if it obviously follows the gas concentration toward the two IRS1 and IRS2 protoclusters and the "Y"-shaped filament. The YSOs themselves cluster in three places: strongly around the IRS1 and IRS2 protoclusters and more distributed around the S Mon massive star.

Table 3 lists the number of YSOs regardless of their class, the number of Class 0/I protostars and Class II pre-main sequence stars found by Rapson et al. (2014) in NGC 2264. We distributed this YSO population among the three subregions of the NGC 2264 cloud defined in Section 3.1. Unlike the spatial distribution of clumps in subregions, a very uneven distribution is observed for the YSOs. The central subregion, which accounts for 22% of the whole NGC 2264 cloud area and contains 38% of the detected clumps (see Tables 2 and 3) indeed gathers up to 62% (302 out of 485) of the YSO population. In contrast, the southern subregion, which covers 45% of the whole cloud, contains 33% of the clumps but only 6% (27 out of 485) of the YSOs. This clear lack of YSOs in this subregion cannot be explained by the small area of the *Herschel* image not investigated for YSOs by Rapson et al. (2014) (see Fig. 12). The northen subregion show a more balanced distribution with 33%, 29%, and 32% of the cloud area, clump and YSO populations.

Regarding the evolutionary class of YSOs, the northern subregion is almost exclusively populated by Class II sources (146 out of 156, 95%, see Table 3). On the other hand, the distribution is more balanced in the central and southern subregions: 23%-30% of the YSOs are Class 0/I protostars and the complementary 70-77% are Class II sources. Finally, we found that the 69 Class 0/I in the central subregion represent a large majority (79%, see Table 3) of this younger YSO population in the whole NGC 2264 cloud.

5.2. Link between the clump and YSO populations

We investigated the spatial correlation between the clump and YSO populations found in the different subregions of NGC 2264 using the nearest neighbor statistics. Figures 13a-d show the distributions of the distance to the first nearest neighbor (nnd) from YSOs to clumps and vice versa, with YSO populations separated into Class 0/I protostars and Class II pre-main sequence stars. Class-0/I and clumps are similarly distributed in the northern and southern subregions (see Table 3 and Fig. 12), in addition the nnd distributions between Class-0/I and clumps cannot be statistically distinguished, according to a KS test. We therefore combined the northern and southern populations of Class 0/I protostars to increase the sample size (18 objects). The 10 clumps detected in the *Herschel* area not covered by *Spitzer* (see Fig. 12 and Table 3) and thus not surveyed for YSOs by Rapson et al. (2014) have been excluded from our analysis.

The nearest neighbor distance, *nnd*, distribution between Class 0/I protostars and clumps first illustrates the strong link between Class 0/I protostars and their parental clump. Indeed,

the large majority, $80 - 95\%$, of the Class 0s/Is of each of the NGC 2264 subregions lie at a distance smaller than the median outer radius of clumps, i.e. below 0.25 pc (see Fig. 13a). Conversely, the *nnd* distribution of clumps with respect to Class 0/I protostars shows in Fig. 13b that ~40% of the clumps in the central subregion host, within their outer radius, at least one Class 0/I protostar. This fraction raises to 2/3 when considering only bound clumps in the central subregion. In addition to illustrating this parental link, the *nnd* distributions between clumps and Class 0s/Is presents, for both the central and northern + southern samples a peak around 1 pc (see Fig. 13b). This peak shows that aside the population of clumps tightly linked to Class 0/I, mostly clustered in the central region, there exists all over NGC 2264 a disperse population of clumps that are not associated to Class 0/I YSOs. As a matter of fact, most of the clumps that create this peak, ~75% whatever the subregion, are qualified as unbound. These unbound clumps could be more than transient cloud fragments because the external gas pressure associated with the global collapse is not taken into account in the calculation of gravitational boundedness. Excluding clumps presently qualified as unbound however, the *nnd* distribution between clumps and Class 0s/Is still displays a peak, which is weaker and located at ~0.5 pc.

Figures 13c-d display the *nnd* distributions between clumps and Class II pre-main sequence stars. Given the proper motions found by Buckner et al. (2020) for the weakly embedded Class II sources in the NGC 2264 cloud, ~1 mas yr^{-1}, and their estimated age, $\sim \times 10^6$ yr Venuti et al. (2018), they could have dispersed by ~6 pc from their original birth site. For these Class II sources, we thus do not expect a direct parental link between Class IIs and the presently observed clumps. Other Class II pre-main sequence stars could well remain more tightly associated with their birth site, like it is probably the case in the NGC 2264 IRS1 and IRS2 protoclusters. The histograms of Figs. 13c-d should thus reveal the parental link of a clustered population of Class IIs plus the average spatial distributions of a more extended population of Class IIs, with no direct parental link with clumps. If the small number, 19, of Class II YSOs in the southern subregion makes any detailed characterization of the histogram shown in Fig. 13c not relevant, that of Fig. 13d should be robust to interpret. While the *nnd* distributions between clumps and Class II sources are similar in the central and northern subregions, the one of the southern subregion clearly stands out as different (see Fig. 13d). The former are both broadly distributed around ~0.2 pc.

In contrast, in the southern subregion, the *nnd* distribution between clumps and Class IIs presents a strong peak at ~1 pc, which means at much further distances than in the other parts of the cloud. This definitively is a consequence of the low density of YSOs observed in the southern subregion (see Fig. 12). One can question the association of Class IIs with the southern subregion or even their membership in the NGC 2264 cloud. Indeed, with proper motions like those measured by Buckner et al. (2020), the Class IIs observed in the southern subregion could have formed in, and been ejected from, the central subregion of NGC 2264. As a guideline, Buckner et al. (2020) also estimated that up to 30% of the YSOs observed in the area covered by the NGC 2264 cloud may not be members of this star-forming region. A detailed comparison of the star and cloud velocities measured with ground-based radiotelescopes and the *gaia* observatory would be necessary to evaluate the YSO membership in the southern subregion of NGC 2264.

The comparison of the *nnd* distributions of clumps with respect to YSOs (see Figs. 13b and 13d), in the central and northern subregions, leads to an apparent counter-intuitive result. On
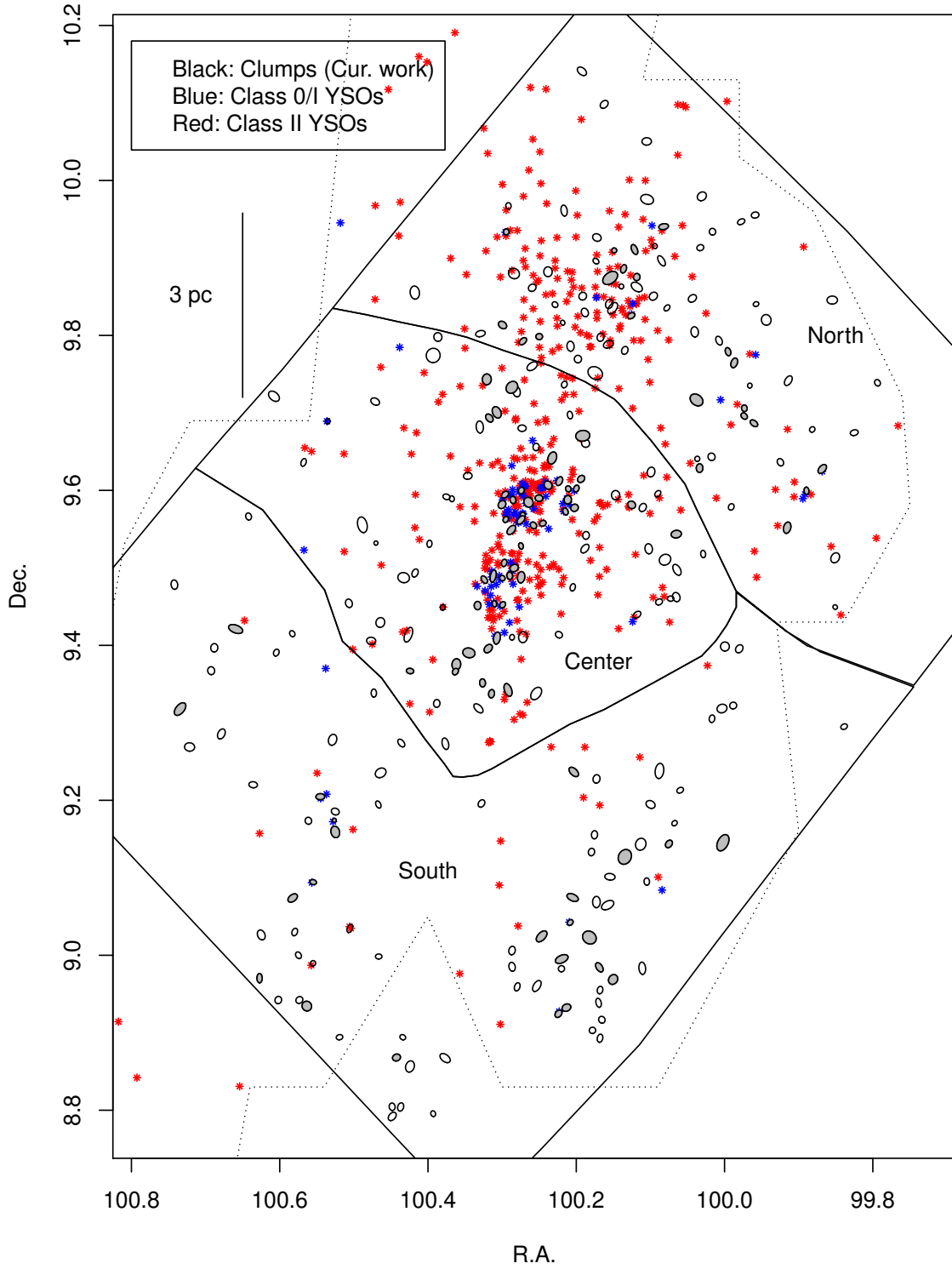
Fig. 12: Spatial distribution of the clump (black ellipses) and YSO populations in the NGC 2264 cloud, as taken from the catalogs of Table 1 and Rapson et al. (2014). Bound clumps are represented with filled ellipses. Class 0/I (blue star markers) and Class II (red star markers) sources were identified in the area outlined by black dotted lines. The three subregions of NGC 2264 (see Section 3.1) are outlined and labeled in black. Clumps are much more homogeneously distributed over the NGC 2264 cloud than YSOs.

average, clumps are closer to Class II pre-main sequence stars than to Class 0/I protostars: median *nnd* of 0.2 pc versus ≃0.8 pc. This reflects the differences in the spatial distribution visible in Fig. 12: while Class 0s/Is are, for their large majority, clustered in the IRS1 and IRS2 protoclusters, Class IIs and clumps dis-

play a more distributed population. This is totally inconsistent with scenarios of quiet cloud formation followed by a continuous process of star formation (see, e.g., Shu et al. 1987; Krumholz 2014).
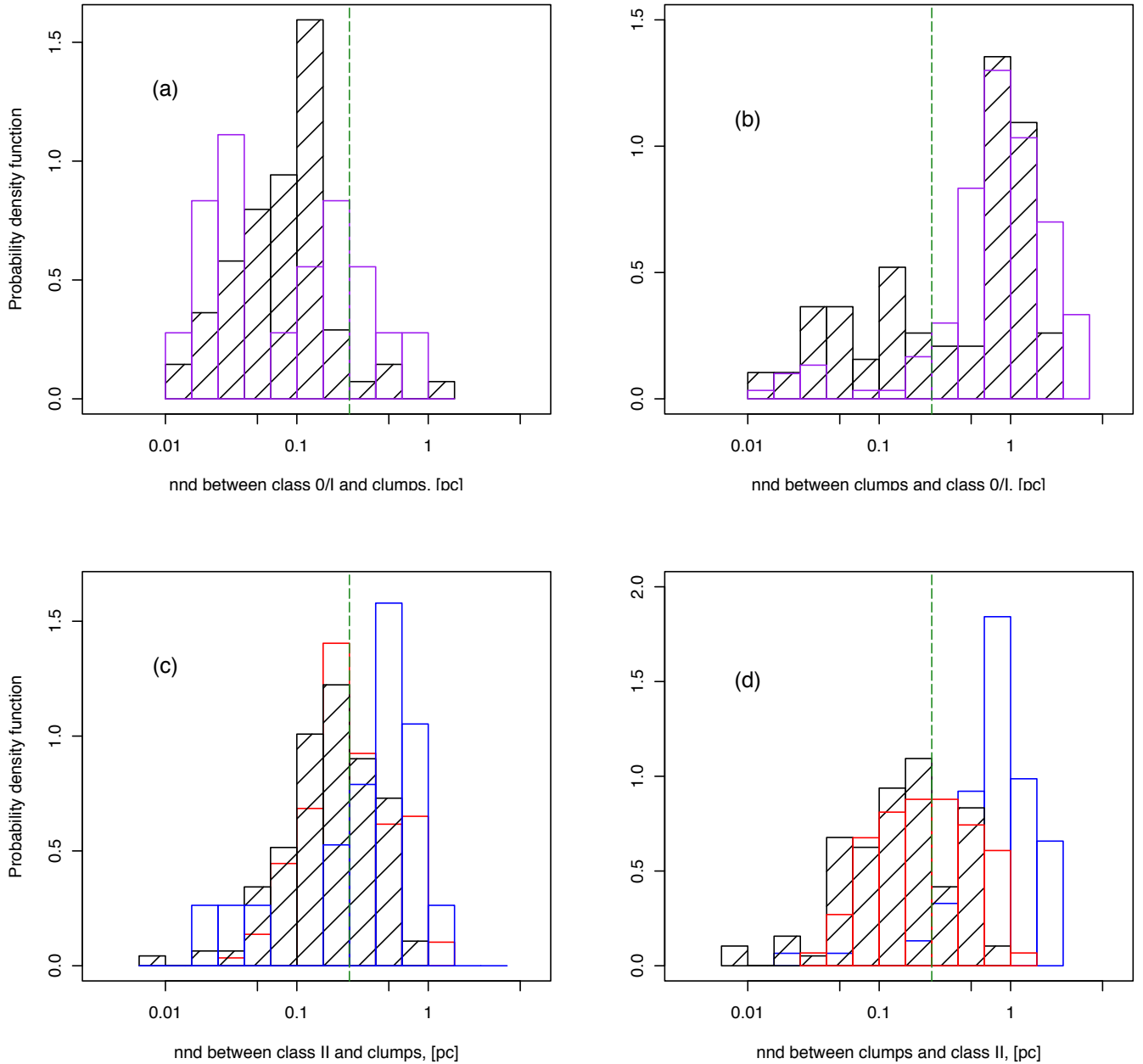
Fig. 13: Distribution of the distance to the first nearest neighbor, *nnd*, from YSOs to clumps (in **a** and **c**) and from clumps to YSOs (in **b** and **d**). YSOs are Class 0/I in the upper panel (**a-b**), Class II in the lower panel (**c-d**). Distributions are presented for the central subregion (black hatched histograms) and for the northern and southern subregions, combined in the upper panel (purple histogram) and separated in the lower panel (red and blue histograms, respectively). Distributions have been normalised to facilitate the comparison involving small populations of YSOs (Class 0/I from northern and southern subregions in **a**, Class II from southern subregions in **c**). The red dashed vertical line indicates the median outer radius of clumps, calculated as twice the median FWHM: $R_{\mathrm{out}}^{\mathrm{med}} = 2\,FWHM^{\mathrm{med}} = 0.25$ pc.

6. Discussion

We hereafter make the link between evidence for mass segregation observed for NGC 2264 clumps and the cloud structure (see Section 6.1) and propose an updated scenario for the star and thus cloud formation history in NGC 2264 (see Section 6.2).

6.1. Mass segregation of clumps and its relationship to cloud structure

Mass segregation has been studied extensively in stellar clusters for decades. More recently, mass segregation has been in-

vestigated for cloud fragments with 0.002 pc to 0.1 pc sizes, using tools developed for stellar clusters. In particular, Dib & Henning (2019) calculated the mass segregation ratio of cores in four star-forming regions: Taurus, Aquila, Corona Australis, and W43-MM1. They found no mass segregation in Taurus but a significant level of mass segregation in the three other clouds: Λ_{MSR} up to 4-9 for the 6–14 most massive cores. Plunkett et al. (2018) also reported that Serpens South is mass segregated, with a median $\Lambda_{\mathrm{MSR}} \simeq 4$ for the $N_{\mathrm{MST}} \leq 18$ most massive cores. Parker (2018) and Könyves et al. (2020) in Orion B, Román-Zúñiga et al. (2019) in Orion A, Sadaghiani et al. (2020) in NGC

6334 also claimed to find mass segregation, although with lower values ($\Lambda_{MSR} \simeq 2 - 3$) and/or involving a smaller number of cores. Besides, no significant mass segregation was found in 12 infrared-dark clouds by Sanhueza et al. (2019). As for the surface density parameter, Σ_j, sometimes used to quantify mass segregation, it was up to now only computed for a couple of star-forming regions. Lane et al. (2016), Parker (2018) and Dib & Henning (2019) notably reported tentative trends for the most massive cores in Orion-A, Orion B, and Corona Australis to sit in areas of higher local surface density. In particular, Lane et al. (2016) found in Orion B a median Σ_{10} value twice larger for the 10 most massive cores than for the whole source samples.

When comparing these published results with the mass segregation found in NGC 2264 (see Section 4.5), the latter is among the strongest and affecting the largest numbers of objects. The Λ_{MSR} parameter is indeed measured to be $\Lambda_{MSR} \simeq 8$ for the $N_{MST} = 4$ to 15 most massive clumps (see Table 3 and Fig. 11a). Moreover, mass segregation remains significant for the ~30 most massive clumps of the NGC 2264 cloud. When the mass segregation is measured by the local surface density, it has a median Σ_6 value for the 15 most massive clumps four times larger than that of the whole sample. We refrained making more quantitative comparisons with published studies since the Λ_{MSR} values are measured with different methods (e.g., sliding window in Román-Zúñiga et al. 2019; Könyves et al. 2020 instead of cumulative form here) and datasets are inhomogeneous. Sources were indeed extracted with different extraction tools (e.g., clumpfind in Román-Zúñiga et al. 2019, FellWalker in Parker 2018 versus *getsf* here) and thus have various definitions. The cloud fragments considered also have different physical sizes, which range from ~0.002 pc (or ~400 AU) in Plunkett et al. (2018), 0.01-0.03 pc (or 2000-6000 AU) in Dib & Henning (2019) to ~0.1 pc (or ~2×10^4 AU) in the present study. Moreover, there are also issues, generally not taken into account, related to the incompleteness of samples and crowding of sources in measuring the mass segregation in dense environments like massive (proto)clusters (Ascenso et al. 2009).

As shown in Fig. 11b, this strong mass segregation is entirely due to the concentration of high-mass clumps in the NGC 2264-IRS1 and IRS2 protoclusters, in the central subregion. We showed that these high-mass clumps all are gravitationally bound and lie at short distance from each other (see Sections 4.3-4.4 and Fig. 3), thus forming a cluster of star-forming clumps. The overabundance of high-mass clumps in the central subregion of NGC 2264 relative to the northern and southern subregions is consistent with its greater gas concentration. After removing clumps from the column density image of Fig. 2, the average column density of this background, at the location of clumps, is indeed almost twice higher in the central subregion than in the other NGC 2264 subregions (see Table 2). The relation between the mass of cloud fragments and their surrounding gas has been reported for several star-forming regions (e.g., Könyves et al. 2020) and presents here a linear correlation between the mass of NGC 2264 clumps, M, and the column density of their surrounding background, $N_{H_2}^{back}$ (see Fig. A5). The incompleteness level of the clump sample could however partly explain this linear correlation and especially the lack of low-mass clumps over regions with high background level.

The overabundance of high-mass clumps in the central subregion is also in line with the fact that its hierarchical structure is different from that of the northern and southern subregions (see Section 3.2). Indeed, the power spectrum of the central subregion, which is hundred times stronger, in fact consists of the sum of a powerlaw function plus power excesses at the scales

of cloud and clump mass reservoirs (see Fig. 6b and Table 2). While diffuse clouds and Gould Belt clouds generally have simple multi-fractal power spectra (Robitaille et al. 2019, 2020), those of high-mass star-forming regions are more complex and dominated, at given scales, by large gravity potentials such as hubs and ridges (Robitaille et al. in prep.). Following the definition criteria set in HOBYS articles (e.g., Hill et al. 2011; Hennemann et al. 2012; Nguyen Luong et al. 2013) and precursor papers (Schneider et al. 2010), the central part of the central subregion of NGC 2264 indeed qualifies as a ridge. In short, ridges are very dense, $>10^5$ cm^{-3}, ~1 pc cloud structures actively forming clusters of intermediate- to high-mass stars (Motte et al. 2018). The center of NGC 2264 indeed hosts a dense north-south filament, which appears as a privileged site for intermediate- to high-mass star formation (see Figs. 3 and 12). It contains a cluster of massive clumps hosting protostars, which could ultimately form a rich YSO cluster with at least a handful of high-mass stars. The mass segregation observed for the NGC 2264 clumps could thus be at the origin of the mass segregation of future stars in, at least, the central stellar cluster of NGC 2264.

We postulate that this mass segregation could come from further afield, in the very way the mass of gas was assembled to form the molecular cloud in the NGC 2264 region. The large-scale kinematics observed throughout the Monoceros cloud complex (Loren 1977; Montillaud et al. 2019) and the global infall discovered toward the NGC 2264-IRS1 protocluster (Williams & Garland 2002; Peretto et al. 2006) indeed suggest that a hierarchical collapse of the NGC 2264 cloud could have led to the formation of a ridge at its center. Further studies of the cloud kinematics are necessary to investigate whether the three filaments that appear converging toward the central ridge, drive material and therefore feed the ridge and its protoclusters. This mode of cloud and thus star formation by competitive, inflowing gas is advocated in theories of hierarchical global collapse (e.g., Vázquez-Semadeni et al. 2019), gravitationally-driven gas inflows (e.g., Smith et al. 2009; Hartmann et al. 2012), filament or conveyor-belt collapse (Myers 2009; Krumholz & McKee 2020) and colliding flows (e.g., Heitsch et al. 2008).

6.2. Star formation history in NGC 2264

Evidence for sequential star formation in NGC 2264 has been presented by several YSO studies (Sung & Bessell 2010; Teixeira et al. 2012; Rapson et al. 2014; Venuti et al. 2018). Venuti et al. (2018) proposed that star formation began ~5 Myr ago in the northern subregion and more precisely in the S Mon area. Then, less than 1 Myr ago, star formation could have developed in the central subregion and especially in the NGC 2264-IRS1 and IRS2 protoclusters. In the present study, this age gradient is qualitatively confirmed when comparing YSO distributions of the northern and central subregions. The central subregion indeed concentrates about 80% of the total Class 0/I protostars of the NGC 2264 cloud while the northern subregion is mainly populated by Class II pre-main sequence stars (see Table 3 and Section 5.1). As for the southern subregion of the NGC 2264, it has not been considered in YSO studies because it contains very few YSOs, only 6% of the total population, suggesting that star formation has not yet been active there. In order to more accurately compare subregions, Fig. 14 displays, for each YSO (Class II and Class 0/I) population, their surface density divided by their statistical lifetime. Surface densities, Σ_{object}, are calculated using the number of objects in each YSO class and the subregion surfaces listed in Tables 2 and 3. We assumed lifetimes, τ_{object},
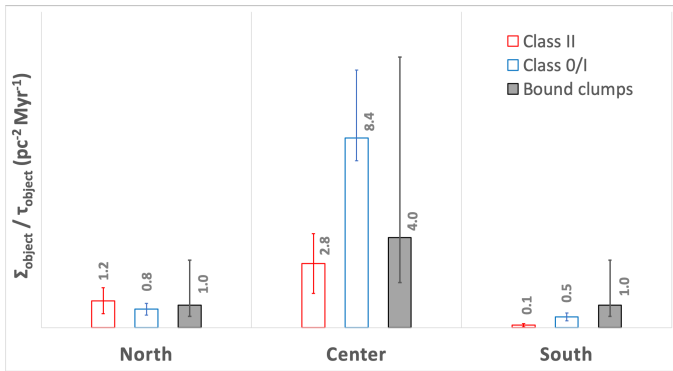
Fig. 14: Surface density per lifetime, $\Sigma_{\text{object}}/\tau_{\text{object}}$, of Class II YSOs, Class 0/I protostars, and clumps in the three NGC 2264 subregions. Statistical lifetimes of 2, 0.2 and 0.3 Myr were assumed for Class IIs, Class 0/Is, and clumps, respectively. Error bars take into account statistical uncertainties, contamination level of 30% for Class IIs, an incompleteness level of 25% for the Class 0/I population in the central subregion, and a factor of two of uncertainty for the clumps. While the star formation activity of the northern subregion appears to be constant, it displays a burst in the central subregion and shows a tentative increase in the southern subregion.

of 2×10^5 yr and 2×10^6 yr for Class I protostars and Class II pre-main sequence stars, respectively, in agreement with Evans et al. (2009), Venuti et al. (2018) and references therein. Error bars on $\Sigma_{\text{object}}/\tau_{\text{object}}$ take into account statistical uncertainties, as well as an estimation of potentially undetected Class 0/Is in the central region and field contamination of Class II population (see Section 5.2 and Buckner et al. 2020). The surface densities per lifetime of Class IIs and Class 0/Is are similar in the northern subregion. This behavior is consistent with the idea that a continuous star formation activity has developed in the northern part of NGC 2264 over the past few 10^6 years. In contrast, in the central and southern subregions, the surface densities per lifetime are $3-5$ times larger for Class 0/I protostars than those measured for Class IIs, suggesting an increase of the star formation activity over the past few 10^5 years.

Identifying and characterizing the ~ 0.1 pc clumps in NGC 2264, using its *Herschel* column density image, allows, for the first time, to study the gas mass reservoir for current and future star formation in the NGC 2264 cloud. In particular, bound clumps represent structures that are forming or will likely form stars in the near future. The clump lifetime is not as properly defined as the one of YSOs but, with a median density of $\sim 8 \times 10^3$ cm^{-3}, they could live for one free-fall time, i.e. $\sim 3 \times 10^5$ yrs. With the goal to further characterize the relative star formation activity in the NGC 2264 cloud, Fig. 14 displays the surface density per lifetime of bound clumps, as measured in the three subregions of NGC 2264. We estimate that the $\Sigma_{\text{clump}}/\tau_{\text{clump}}$ values are uncertain by a factor of at least two. Indeed, as the median densities of clumps vary by a factor of 2 depending on the subregions, the clump free-fall time is thus uncertain by a factor of $\sim 50\%$. Other sources of uncertainty are the number of protostars that will form in each clump, here taken as one, and the number of free-fall times, here assumed to be one, required for these clumps to form stars. With our current assumptions, the surface density per lifetime of clumps is similar to that of YSOs in the northern subregion, implying a continuous star formation activity. In contrast in the southern subregion, Fig. 14 suggests a tentative increase of the surface density per

lifetime of clumps compared to that of the YSOs and therefore a possible increase of the star formation activity from 10^6 years ago to the next few 10^5 years. In the central subregion, uncertainties are too large to conclude that there is any trend for the future star formation activity relative to the current one. All in one, the spatial distribution of YSO and clump populations suggests that the star formation activity will get more and more intense as we go through the NGC 2264 cloud, from north to south, in the coming $\sim 3 \times 10^5$ years. Star formation first developed mainly in the northern subregion and continues today. Star formation is now extremely active in the central subregion while it was less so in the past. Star formation now begins in the southern subregion and could get more active while it was almost nonexistent in the past. This time sequence, based on the study of clump and YSO populations, agrees and extends the evolutionary sequence proposed by, e.g., Venuti et al. (2018).

We propose here that this sequence of star formation is related to a prior sequence of cloud formation, first in the north, now in the center and in the future in the south of NGC 2264. With its large mass reservoir at pc scale (see Table 2), the central subregion, and especially its ridge, has a very large potential for new events of star formation. The cloud power spectrum of the central subregion, and especially its coherent component associated to star formation, also implies that the cloud reservoir for star formation will remain important or will even increase in the coming 10^6 years (see Fig. 6b). Indeed, the coherent component of the cloud contains almost all the power and thus most of the gas mass reservoir in the central subregion (see Figs. 6a-b, Fig. 14 and Table 2). Interestingly, this fraction of coherent cloud structures supposedly associated with star formation is orders of magnitude larger in the central subregion of NGC 2264 than in the northern and southern subregions. The southern subregion has similar properties with respect to its gas distribution (column density and power spectrum) than the northern subregion (see Fig. 6b and Table 3). These observations of the gas thus show that the northern and southern subregions should have the same potential for future star formation events, i.e. similar numbers of stars that could form in the coming $\sim 10^6$ years. This is also consistent with the similarity observed in term of mass, boundedness, and surface density (see Fig. 14 and Table 3). We therefore propose that the NGC 2264 cloud initially concentrated in the northern region several Myrs ago. The cloud distribution in the central subregion makes a strong case for extremely active cloud formation activity now and possibly in the coming 10^6 years. As for the southern subregion, cloud is not yet highly concentrated but it could be enhanced in the close future. Kinematical studies of the the NGC 2264 cloud are obviously necessary to confirm this last assertion.

Over the past few Myr, the NGC 2264 cloud has thus undergone several episodes of cloud and thus star formation. We showed in Section 5.2 that a large fraction of clumps in the NGC 2264-IRS1 and IRS2 protoclusters are the parental cloud structures from which the Class 0/I protostars currently gather their mass. In addition, a population of clumps is observed at large, ~ 1 pc, distances from the current sites of star-formation activity (see Fig. 12 and Fig. 13b). These clumps are smaller in mass and mostly unbound. They thus need to gather more mass and concentrate themselves before they could be considered as the cloud structures that will form new protostars. Future star-formation episodes could develop either aside the current star-formation sites or clumps must first be driven toward them. The population of clumps also appears to be spatially well correlated with Class II pre-main sequence stars, surprisingly better than with Class 0/I protostars. These elements argue for a dy-

namical scenario of star formation in NGC 2264. We speculate that, first and simultaneously, the cloud undergoes global collapse and clumps converge toward the central gravity potentials, called ridges, reducing their distance to star-forming sites. Protostellar collapse would then form a cluster of stars with a definite mass segregation at birth. The last phase would then be for at least part of the population of pre-main sequence stars to disperse from their original birth sites and spread over the entire extent of the NGC 2264 cloud, thus simulating a tight spatial correlation with a new generation of clumps. Whether the most massive and most clustered protostars, embedded within cloud ridges will become closely-packed main sequence stars will define if mass segregation is determined at birth in NGC 2264 and potentially in other dynamical clouds. This scenario is consistent with the finding of Buckner et al. (2020) that YSOs with increasing evolutionary stages tend to be less clustered. It would also qualitatively agree with numerical simulations of cloud formation through, e.g., the hierarchical global collapse (Vázquez-Semadeni et al. 2019) and stellar cluster evolution with the ejection of many YSOs members (Oh & Kroupa 2016).

7. Conclusions

We used an *Herschel* column density image of the NGC 2264 cloud to identify and characterize its clumps, study their spatial distribution, and make the link of these clumps with the YSO population and cloud structure. Our main results can be summarized as follows:

1. We applied *getsf* to the 18.2″-angular resolution column density image. We found a population of 256 clumps with ~0.1 pc sizes, ~14 K temperature and masses ranging from 0.08 $M_\odot$ to 53 $M_\odot$. 36% of the NGC 2264 clumps are gravitationally bound following the Bonnor-Ebert criterium.

2. After analyzing the cloud structure, we divided the NGC 2264 cloud into three subregions (northern, central, and southern) of roughly similar areas. The MnGseg technique revealed that the coherent cloud component associated to star formation dominates over the Gaussian component, especially for the central subregion. We qualified as a ridge the cloud structure at the center of the central subregion of NGC 2264 because it is massive and hosts the NGC 2264-IRS1 and IRS2 protoclusters.

3. We then applied the *nnd* statistics to characterize the spatial distribution of clumps in the NGC 2264 cloud. The majority of the clumps are low-mass, unbound structures distributed all over the cloud. In addition, we found within the NGC 2264 ridge a cluster of higher-mass, bound clumps. The typical distance between clumps in this second population is half that found elsewhere.

4. We quantified the mass segregation of NGC 2264 clumps using two complementary methods. The 15 most massive clumps, with $M = 9.3 - 53\ M_\odot$ and all located in the central protoclusters, have a median local surface density, Σ_6, three times that of the entire clump population. This high degree of mass segregation is also indicated by the strong mass segregation ratio: $\Lambda_{MSR} \simeq 8$ for the $N_{MST} \leq 15$ most massive clumps. We propose that this mass segregation is due to the presence and therefore to the formation of a ridge by the global collapse of clouds in the central subregion of NGC 2264.

5. Except for those in the ridge, most of the clumps in the NGC 2264 cloud are not associated with Class 0/I protostars.

At odd with what a parental link would suggest, *nnd* distributions notably show that the spatial distribution of clumps better correlates with that of Class II pre-main sequence stars. This argues for a dynamical scenario where clumps are driven to the central parts of the NGC 2264, protostars are formed in situ, and some Class IIs are ejected from their birth site.

6. Our combined study of clump and YSO populations in NGC 2264 agrees and extends the sequential star formation sequence from north to south, which was initially proposed by YSO studies. Star formation first developed in the northern subregion. It is now extremely active in the central subregion and should soon begin in the southern subregion. We propose to explain it by a sequence of cloud formation from north to south.

The strong mass segregation observed for the NGC 2264 clumps, which is most likely due to the formation of a favorable cloud structure, the ridge, could itself be at the origin of future mass segregation in the NGC 2264 stellar cluster. Detailed studies of the cloud and YSO kinematics are mandatory to confirm our current interpretation and predictions.

References

Allison, R. J., Goodwin, S. P., Parker, R. J., et al. 2009, MNRAS, 395, 1449
André, P., Men'shchikov, A., Bontemps, S., et al. 2010, A&A, 518, L102
Ascenso, J., Alves, J., & Lago, M. T. V. T. 2009, A&A, 495, 147
Buckner, A. S. M., Khorrami, Z., González, M., et al. 2020, A&A, 636, A80
Cantat-Gaudin, T., Jordi, C., Vallenari, A., et al. 2018, A&A, 618, A93
Cartwright, A. & Whitworth, A. P. 2004, MNRAS, 348, 589
Casertano, S. & Hut, P. 1985, ApJ, 298, 80
Cody, A. M., Stauffer, J., Baglin, A., et al. 2014, AJ, 147, 82
Cunningham, N., Lumsden, S. L., Cyganowski, C. J., Maud, L. T., & Purcell, C. 2016, MNRAS, 458, 1742
Dahm, S. E. 2008, The Young Cluster and Star Forming Region NGC 2264, ed. B. Reipurth, Vol. 4, 966
Dib, S. & Henning, T. 2019, A&A, 629, A135
Dib, S., Schmeja, S., & Parker, R. J. 2018, MNRAS, 473, 849
Didelon, P., Motte, F., Tremblin, P., et al. 2015, A&A, 584, A4
Evans, Neal J., I., Dunham, M. M., Jørgensen, J. K., et al. 2009, ApJS, 181, 321
Fujii, M. S. & Portegies Zwart, S. 2016, ApJ, 817, 4
Griffin, M. J., Abergel, A., Abreu, A., et al. 2010, A&A, 518, L3
Gutermuth, R. A., Megeath, S. T., Myers, P. C., et al. 2009, ApJS, 184, 18
Hartmann, L., Ballesteros-Paredes, J., & Heitsch, F. 2012, MNRAS, 420, 1457
Heitsch, F., Hartmann, L. W., Slyz, A. D., Devriendt, J. E. G., & Burkert, A. 2008, ApJ, 674, 316
Hennemann, M., Motte, F., Schneider, N., et al. 2012, A&A, 543, L3
Hetem, A. & Gregorio-Hetem, J. 2019, MNRAS, 490, 2521
Hill, T., Motte, F., Didelon, P., et al. 2011, A&A, 533, A94
Hill, T., Motte, F., Didelon, P., et al. 2012, A&A, 542, A114
Juvela, M., Ristorcelli, I., Pagani, L., et al. 2012, A&A, 541, A12
Kirby, J. F. 2005, Computers and Geosciences, 31, 846
Könyves, V., André, P., Arzoumanian, D., et al. 2020, A&A, 635, A34
Krumholz, M. R. 2014, Phys. Rep., 539, 49
Krumholz, M. R. & McKee, C. F. 2020, MNRAS, 494, 624
Kuhn, M. A., Feigelson, E. D., Getman, K. V., et al. 2014, ApJ, 787, 107
Lane, J., Kirk, H., Johnstone, D., et al. 2016, ApJ, 833, 44
Loren, R. B. 1977, ApJ, 215, 129
Maschberger, T. & Clarke, C. J. 2011, MNRAS, 416, 541

Maury, A. J., André, P., & Li, Z. Y. 2009, A&A, 499, 175

Men'shchikov, A. 2013, A&A, 560, A63

Men'shchikov, A. 2017, A&A, 607, A64

Men'shchikov, A., André, P., Didelon, P., et al. 2012, A&A, 542, A81

Meylan, G. 2000, in Astronomical Society of the Pacific Conference Series, Vol. 211, Massive Stellar Clusters, ed. A. Lançon & C. M. Boily, 215

Montillaud, J., Juvela, M., Vastel, C., et al. 2019, A&A, 631, A3

Motte, F., Bontemps, S., & Louvet, F. 2018, ARA&A, 56

Motte, F., Zavagno, A., Bontemps, S., et al. 2010, A&A, 518, L77

Murray, S. D. & Lin, D. N. C. 1996, ApJ, 467, 728

Myers, P. C. 2009, ApJ, 700, 1609

Nguyen Luong, Q., Motte, F., Carlhoff, P., et al. 2013, ApJ, 775, 88

Nguyen Luong, Q., Motte, F., Hennemann, M., et al. 2011, A&A, 535, A76

Oh, S. & Kroupa, P. 2016, A&A, 590, A107

Ott, S. 2010, in Astronomical Society of the Pacific Conference Series, Vol. 434, Astronomical Data Analysis Software and Systems XIX, ed. Y. Mizumoto, K. I. Morita, & M. Ohishi, 139

Palmeirim, P., André, P., Kirk, J., et al. 2013, A&A, 550, A38

Parker, R. J. 2018, MNRAS, 476, 617

Parker, R. J. & Goodwin, S. P. 2015, MNRAS, 449, 3381

Parker, R. J., Goodwin, S. P., Wright, N. J., Meyer, M. R., & Quanz, S. P. 2016, MNRAS, 459, L119

Parker, R. J. & Meyer, M. R. 2012, MNRAS, 427, 637

Peretto, N., André, P., & Belloche, A. 2006, A&A, 445, 979

Peretto, N., Fuller, G. A., Duarte-Cabral, A., et al. 2013, A&A, 555, A112

Plunkett, A. L., Fernández-López, M., Arce, H. G., et al. 2018, A&A, 615, A9

Poglitsch, A., Waelkens, C., Geis, N., et al. 2010, A&A, 518, L2

Povich, M. S., Kuhn, M. A., Getman, K. V., et al. 2013, ApJS, 209, 31

Rapson, V. A., Pipher, J. L., Gutermuth, R. A., et al. 2014, ApJ, 794, 124

Rayner, T. S. M., Griffin, M. J., Schneider, N., et al. 2017, A&A, 607, A22

Rivera-Ingraham, A., Martin, P. G., Polychroni, D., et al. 2013, ApJ, 766, 85

Robitaille, J.-F., Abdeldayem, A., Joncour, I., et al. 2020, arXiv e-prints, arXiv:2007.08206

Robitaille, J.-F., Joncas, G., & Miville-Deschênes, M.-A. 2014, MNRAS, 440, 2726

Robitaille, J. F., Motte, F., Schneider, N., Elia, D., & Bontemps, S. 2019, A&A, 628, A33

Román-Zúñiga, C. G., Alfaro, E., Palau, A., et al. 2019, MNRAS, 489, 4429

Roussel, H. 2013, PASP, 125, 1126

Sadaghiani, M., Sánchez-Monge, Á., Schilke, P., et al. 2020, A&A, 635, A2

Sánchez, N. & Alfaro, E. J. 2009, ApJ, 696, 2086

Sanhueza, P., Contreras, Y., Wu, B., et al. 2019, ApJ, 886, 102

Schneider, N., Csengeri, T., Bontemps, S., et al. 2010, A&A, 520, A49

Schneider, N., Csengeri, T., Hennemann, M., et al. 2012, A&A, 540, L11

Schwartz, P. R. 1987, ApJ, 320, 258

Shu, F. H., Adams, F. C., & Lizano, S. 1987, ARA&A, 25, 23

Smith, R. J., Longmore, S., & Bonnell, I. 2009, MNRAS, 400, 1775

Spitzer, Lyman, J. 1969, ApJ, 158, L139

Sung, H. & Bessell, M. S. 2010, AJ, 140, 2070

Sung, H., Bessell, M. S., Chun, M.-Y., Karimov, R., & Ibrahimov, M. 2008, AJ, 135, 441

Sung, H., Stauffer, J. R., & Bessell, M. S. 2009, AJ, 138, 1116

Teixeira, P. S., Lada, C. J., Marengo, M., & Lada, E. A. 2012, A&A, 540, A83

Teixeira, P. S., Lada, C. J., Young, E. T., et al. 2006, ApJ, 636, L45

Tigé, J., Motte, F., Russeil, D., et al. 2017, A&A, 602, A77

Vázquez-Semadeni, E., Palau, A., Ballesteros-Paredes, J., Gómez, G. C., & Zamora-Avilés, M. 2019, MNRAS, 490, 3061

Venuti, L., Prisinzano, L., Sacco, G. G., et al. 2018, A&A, 609, A10

Williams, J. P. & Garland, C. A. 2002, ApJ, 568, 259

Young, E. T., Teixeira, P. S., Lada, C. J., et al. 2006, ApJ, 642, 972
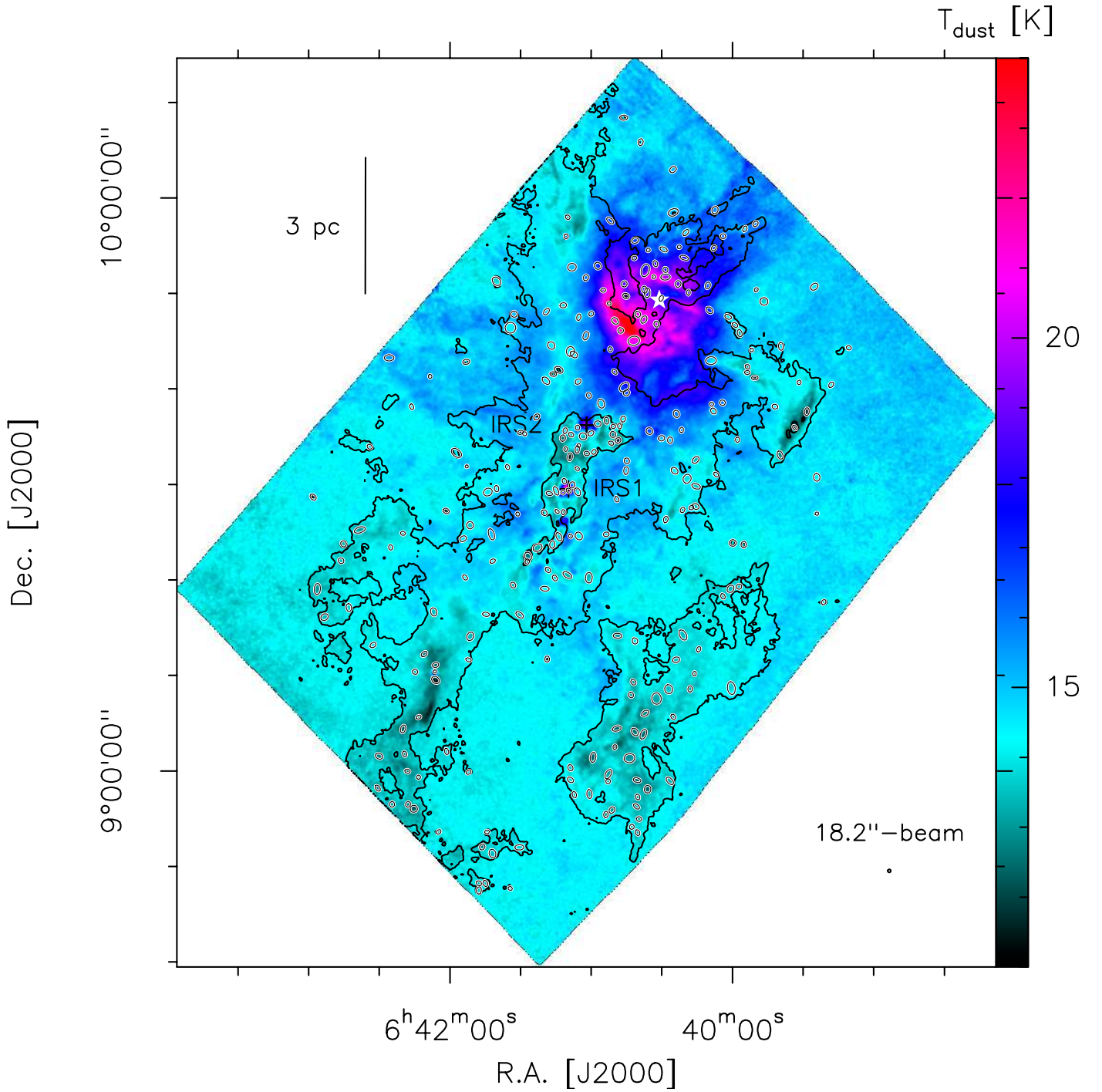
Fig. A1: *Herschel* dust temperature image of the NGC 2264 cloud, with 3.4×10^{21} H_2 cm^{-2} and 1.6×10^{22} H_2 cm^{-2} contours taken from the column density image of Fig. 2. The resolution of the map, 18.2″, is shown in the lower-right corner and a scale bar is given in the upper-left corner. A white star locates the OB star cluster which heats its surrounding cloud over several parsecs. The IRS1 and IRS2 protoclusters are also indicated.
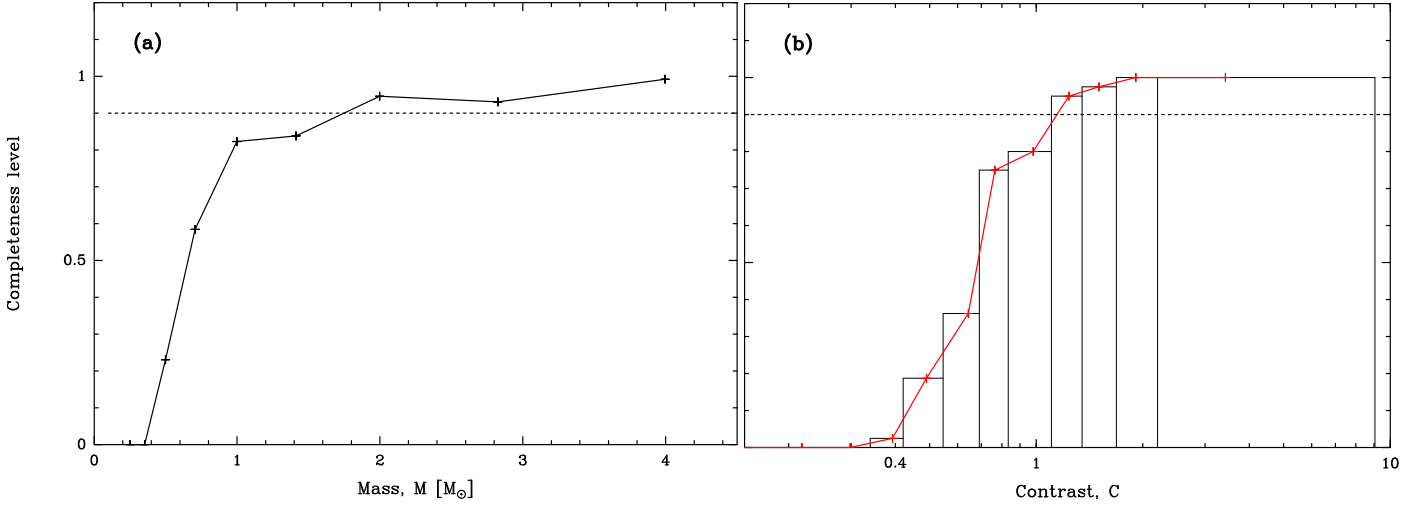
Fig. A2: Completeness level of the clumps extraction as a function of the clump mass (in **a**) and of the contrast of the clump column density over its local background (in **b**). The 90% completeness level is indicated with a dashed horizontal line. **a)** The clump sample is 90% complete above 1.7 $M_\odot$. **b)** The histogram has been constructed with a constant number of 80 synthetic sources in the 11 first bins, plus a bin containing the remaining 290 sources which have all been detected. The red curve connects the median contrast value in each bin. 90% of the clump are detected for a contrast larger than 1.1.
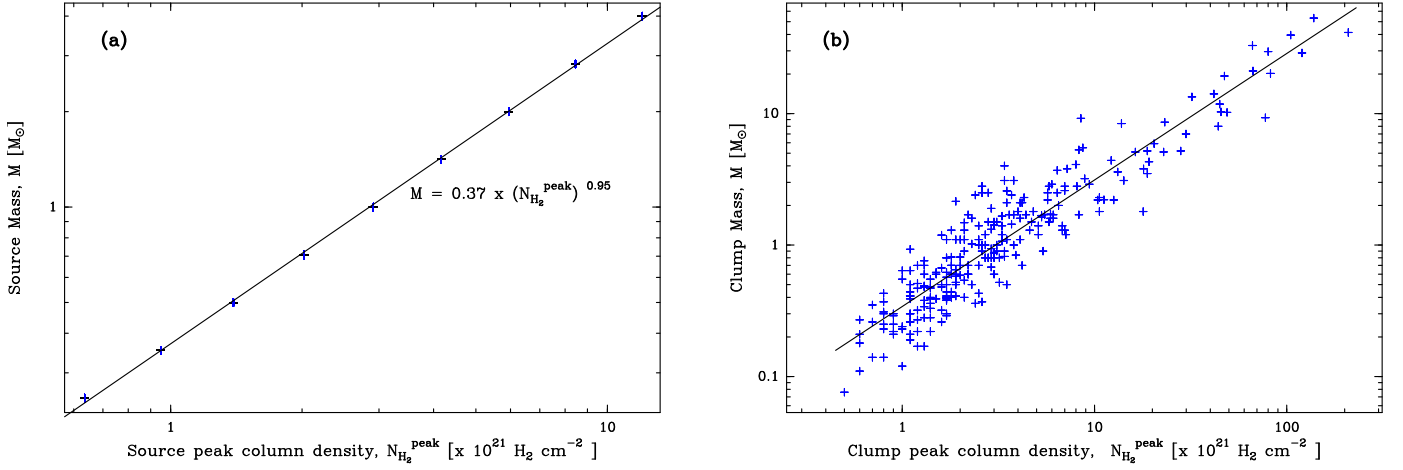
Fig. A3: In relation with the intensity profile of clumps, clump masses are plotted against the peak column density **a)** for synthetic sources and **b)** for observed clumps. A simple regression gives the relation $M = \beta(N_{\mathrm{H2}}^{\mathrm{peak}})^{0.95}$ with $\beta = 0.37$ in **a** over a $[0.6 - 12 \times 10^{21} \text{ cm}^{-2}]$ range, $\beta = 0.34$ in **b** over a $[0.5 - 200 \times 10^{21} \text{ cm}^{-2}]$. The similarity in the fitted parameters confirms that the synthetic sources correctly represent the observed clumps.

Table A1: Catalog of clumps.

#	Alp [J2000]	Del [J2000]	$A \times B$ ["$\times$"]	PA [°]	Sig	$N_{H_2}^{peak}$ [Av units]^a	$N_{H_2}^{int}$ [Av units]^a	FWHM$_{dec}$ ^{b} [pc]	T_{dust} [K]	M [$M_\odot$]	α_{BE}	$N_{H_2}^{back}$ [Av units]^a
1	100.5263	9.1742	18.2 × 18.2	18.3	80.5	18 ± 2	14 ± 2	0.03	20 ± 2	1.8 ± 0.2	0.3	11.5 ± 0.2
2	100.2023	9.5775	36.6 × 32.4	152.2	174.4	80 ± 6	286 ± 10	0.1	11.8 ± 0.3	30 ± 1	0.03	17.4 ± 0.6
3	100.2944	9.9336	27.4 × 26.2	24.5	104.8	19 ± 2	41 ± 2	0.07	15.7 ± 0.7	4.3 ± 0.2	0.21	8.8 ± 0.2
4	99.8894	9.5995	33.6 × 23.2	44.3	94.8	30 ± 3	68 ± 4	0.07	11.5 ± 0.4	7.0 ± 0.4	0.1	13.0 ± 0.3
5	100.2081	9.0423	30.1 × 23.4	168.7	76.2	11.2 ± 0.8	21.0 ± 0.9	0.07	12.3 ± 0.2	2.2 ± 0.1	0.31	6.5 ± 0.1
6	100.2997	9.4868	26.5 × 23.8	93.5	64.4	209 ± 12	400 ± 15	0.06	17.3 ± 0.7	41 ± 2	0.02	61 ± 1
7	100.2741	9.5998	31.3 × 26.3	7.2	56.5	82 ± 11	195 ± 14	0.08	15.0 ± 0.4	20 ± 1	0.05	46 ± 3
8	100.272	9.5686	22.8 × 22.8	22.6	47.7	77 ± 11	90 ± 13	0.05	15.4 ± 0.7	9 ± 1	0.07	52 ± 2
9	100.3104	9.4536	29.5 × 20.2	48.4	50.1	44 ± 8	77 ± 9	0.06	13.3 ± 0.4	8.0 ± 0.9	0.08	22.6 ± 0.6
10	100.5549	9.0945	31.8 × 22.5	115.5	42.3	11 ± 2	22 ± 3	0.07	12.6 ± 0.4	2.3 ± 0.3	0.31	9.7 ± 0.5
11	99.9603	9.6866	40.8 × 24.9	93.2	45.8	13 ± 1	35 ± 1	0.09	12.2 ± 0.2	3.6 ± 0.1	0.26	6.4 ± 0.2
12	99.9953	9.779	38.2 × 25.4	56.7	46.9	5.9 ± 0.2	17.0 ± 0.3	0.09	13.5 ± 0.3	1.7 ± 0.0	0.58	2.9 ± 0.0
13	100.2838	9.4498	41.0 × 32.3	153.3	48.6	138 ± 13	514 ± 21	0.11	16 ± 2	53 ± 2	0.03	41 ± 3
14	100.25	9.7985	31.9 × 27.8	129.0	40.5	5.9 ± 0.9	15 ± 1	0.08	15.1 ± 0.3	1.6 ± 0.1	0.65	7.1 ± 0.2
15	100.224	8.9245	38.6 × 28.0	174.2	44.6	5.3 ± 0.4	16.0 ± 0.6	0.1	13.0 ± 0.2	1.7 ± 0.1	0.61	3.9 ± 0.1
16	100.2746	9.5619	46.7 × 26.6	174.2	32.2	67 ± 11	204 ± 15	0.11	13.7 ± 0.7	21 ± 2	0.06	45 ± 3
17	100.2961	9.5946	37.4 × 25.9	166.2	31.2	46 ± 13	100 ± 13	0.09	14.0 ± 0.9	10 ± 1	0.1	35 ± 3
18	100.1488	9.9097	23.8 × 22.8	113.5	31.8	5 ± 1	9 ± 2	0.05	15.8 ± 0.4	0.9 ± 0.2	0.74	5.2 ± 0.3
19	100.1259	9.8254	37.1 × 24.9	155.3	39.4	6 ± 1	16 ± 2	0.09	16.5 ± 0.3	1.7 ± 0.2	0.69	5.9 ± 0.2
20	100.3121	9.4895	57.4 × 27.1	25.2	36.5	105 ± 13	382 ± 19	0.12	14.3 ± 0.4	40 ± 2	0.04	55 ± 3
21	99.9869	9.7646	46.5 × 29.6	15.4	36.3	4.4 ± 0.3	16.0 ± 0.5	0.11	13.3 ± 0.3	1.7 ± 0.1	0.73	2.9 ± 0.1
22	100.2898	9.4898	33.9 × 26.9	47.0	26.1	120 ± 13	280 ± 14	0.08	22 ± 1	29 ± 2	0.05	54 ± 2
23	100.1215	9.9109	48.7 × 26.4	63.9	45.7	9 ± 1	31 ± 2	0.11	15.0 ± 0.2	3.2 ± 0.2	0.42	6.6 ± 0.2
24*	100.4425	8.868	38.6 × 31.3	143.8	47.3	4.8 ± 0.4	17.0 ± 0.8	0.1	12.6 ± 0.2	1.8 ± 0.1	0.6	3.1 ± 0.1
25	100.2921	9.3425	61.6 × 33.6	59.7	54.6	8 ± 1	39 ± 2	0.15	13.4 ± 0.1	4.1 ± 0.2	0.4	7.5 ± 0.3
26	100.238	9.6068	40.9 × 34.9	82.4	38.8	47 ± 13	186 ± 21	0.12	13.6 ± 0.6	19 ± 2	0.07	31 ± 4
27	100.3241	9.4849	38.9 × 24.1	75.9	28.5	49 ± 13	98 ± 15	0.09	13.4 ± 0.3	10 ± 2	0.09	42 ± 4
28	100.3172	9.6934	42.1 × 29.6	80.3	34.0	8 ± 2	27 ± 3	0.11	13.9 ± 0.2	2.8 ± 0.3	0.44	10.0 ± 0.3
29	100.1688	8.9845	48.3 × 28.3	73.7	40.7	7.0 ± 0.9	27 ± 1	0.11	12.4 ± 0.1	2.8 ± 0.1	0.41	7.4 ± 0.1
30	100.3801	9.449	26.5 × 22.8	25.5	25.6	2.5 ± 0.8	4.0 ± 0.9	0.06	15.6 ± 0.3	0.4 ± 0.1	1.7	3.8 ± 0.1
31	100.0337	9.6287	39.7 × 31.8	36.3	38.8	5.7 ± 0.9	21 ± 1	0.11	14.7 ± 0.2	2.2 ± 0.1	0.59	5.8 ± 0.1
32	99.9659	9.7352	22.7 × 21.9	22.4	25.5	2.6 ± 0.8	4.0 ± 0.9	0.05	13.8 ± 0.2	0.4 ± 0.1	1.4	3.3 ± 0.1
33	100.5634	8.9344	46.5 × 44.0	95.3	50.8	8.7 ± 0.7	53 ± 2	0.15	12.4 ± 0.2	5.5 ± 0.2	0.27	4.2 ± 0.2
34	100.1253	9.5813	38.9 × 33.2	98.1	34.3	6.4 ± 0.8	24 ± 1	0.11	15.1 ± 0.3	2.5 ± 0.1	0.54	7.4 ± 0.1
35	100.0074	9.7932	43.4 × 28.3	65.5	27.8	3.0 ± 0.2	8.0 ± 0.2	0.11	14.2 ± 0.3	0.9 ± 0.0	1.4	3.1 ± 0.1
36	100.2145	9.5727	33.2 × 24.0	61.2	22.6	18 ± 7	36 ± 8	0.08	13.1 ± 0.3	3.8 ± 0.8	0.22	21.9 ± 0.6
37	100.1184	9.8753	33.0 × 31.5	18.7	28.9	6 ± 1	16 ± 2	0.09	17.8 ± 0.5	1.7 ± 0.2	0.81	5.6 ± 0.2
38	100.2994	9.8134	42.3 × 31.2	96.0	28.2	7 ± 1	25 ± 2	0.11	13.8 ± 0.2	2.6 ± 0.2	0.48	8.3 ± 0.2
39	100.2034	9.2366	54.4 × 31.1	86.2	38.4	4.2 ± 0.5	20.0 ± 0.9	0.13	13.0 ± 0.2	2.1 ± 0.1	0.66	5.2 ± 0.1
40	100.2644	9.5847	47.0 × 42.3	75.8	27.5	66 ± 13	318 ± 19	0.14	13.8 ± 0.4	33 ± 2	0.05	54 ± 3
41	100.6272	8.9705	43.1 × 25.2	38.8	34.5	5.3 ± 0.5	16.0 ± 0.6	0.1	12.6 ± 0.2	1.6 ± 0.1	0.62	4.4 ± 0.2
42	100.4702	9.532	19.4 × 19.4	4.4	19.8	1.0 ± 0.1	1.0 ± 0.1	0.03	13.8 ± 0.2	0.1 ± 0.0	3.0	2.5 ± 0.0
43	100.0651	9.5435	49.8 × 34.5	135.0	34.2	3.3 ± 0.5	16.0 ± 0.8	0.13	13.5 ± 0.2	1.7 ± 0.1	0.88	4.2 ± 0.0
44	100.0434	9.8478	42.8 × 31.7	161.1	24.5	3.3 ± 0.9	12 ± 1	0.11	16.2 ± 0.3	1.2 ± 0.1	1.3	4.2 ± 0.1
45	100.075	9.1437	38.5 × 28.8	175.8	23.3	3.3 ± 0.6	10.0 ± 0.9	0.1	13.1 ± 0.1	1.1 ± 0.1	0.99	5.8 ± 0.1
46	100.2876	9.5489	50.5 × 30.1	173.9	21.5	42 ± 6	137 ± 8	0.12	11.8 ± 0.2	14.1 ± 0.8	0.08	31 ± 1
47	100.1391	9.8632	22.8 × 22.8	116.8	18.3	4 ± 1	5 ± 1	0.05	19.8 ± 0.3	0.5 ± 0.1	1.6	6.5 ± 0.2
48	100.2183	9.8165	23.6 × 20.1	70.1	17.4	1.3 ± 0.6	2.0 ± 0.6	0.04	22.7 ± 0.7	0.2 ± 0.1	4.7	3.4 ± 0.1
49	100.0822	9.9404	47.0 × 26.7	136.8	20.7	7 ± 1	19 ± 1	0.11	14.7 ± 0.2	2.0 ± 0.1	0.65	5.1 ± 0.1
50	100.2993	9.4523	31.3 × 24.7	175.5	18.4	19 ± 5	34 ± 5	0.07	13.2 ± 0.4	3.5 ± 0.6	0.23	17.1 ± 0.7
51	100.1999	9.6023	32.3 × 24.7	12.9	18.1	10 ± 3	21 ± 3	0.08	13.8 ± 0.4	2.2 ± 0.3	0.39	13.4 ± 0.4
52	100.2532	8.9604	57.3 × 31.9	4.4	20.2	3.3 ± 0.6	14.0 ± 0.8	0.14	13.3 ± 0.2	1.4 ± 0.1	1.1	4.0 ± 0.2
53	100.1503	8.9688	48.3 × 41.0	176.3	21.7	6 ± 1	27 ± 2	0.14	12.6 ± 0.1	2.8 ± 0.2	0.53	6.3 ± 0.3
54	100.1049	9.0951	34.1 × 26.5	43.2	20.4	2.5 ± 0.8	7 ± 1	0.08	13.2 ± 0.1	0.7 ± 0.1	1.3	4.1 ± 0.2
55	100.3751	9.5917	34.9 × 25.5	111.1	17.1	3.9 ± 0.7	8.0 ± 0.7	0.08	14.5 ± 0.2	0.8 ± 0.1	1.2	5.7 ± 0.0
56	100.118	9.4395	41.1 × 27.4	162.4	17.6	4 ± 1	10 ± 2	0.1	13.5 ± 0.3	1.1 ± 0.2	1.0	5.4 ± 0.1
57	100.3073	9.7007	55.8 × 39.1	66.0	23.9	6 ± 2	36 ± 3	0.15	14.0 ± 0.2	3.7 ± 0.3	0.47	10.5 ± 0.4
58	100.2719	9.7925	40.7 × 25.5	168.4	19.7	4.6 ± 0.8	12 ± 1	0.09	14.5 ± 0.1	1.3 ± 0.1	0.86	8.4 ± 0.2
59	100.2287	9.8397	29.6 × 25.1	92.0	21.3	1.8 ± 0.7	4 ± 1	0.07	19.1 ± 0.5	0.4 ± 0.1	2.8	4.7 ± 0.1
60	100.5452	9.2047	42.5 × 27.9	129.7	17.7	6 ± 3	16 ± 3	0.1	12.7 ± 0.3	1.6 ± 0.3	0.67	7.4 ± 0.6
61	100.4242	9.3669	35.7 × 24.6	119.9	18.9	4 ± 1	9 ± 1	0.08	14.1 ± 0.1	1.0 ± 0.1	0.96	5.7 ± 0.1
62	100.3618	9.3753	52.8 × 41.7	30.6	29.5	14 ± 2	81 ± 4	0.15	12.7 ± 0.2	8.4 ± 0.4	0.19	11.2 ± 0.3
63	100.0883	9.4561	34.2 × 27.1	151.5	20.9	3 ± 1	8 ± 2	0.09	13.4 ± 0.2	0.8 ± 0.2	1.2	4.7 ± 0.2
64	100.2161	9.7366	31.7 × 26.4	7.5	21.2	1.4 ± 0.4	4.0 ± 0.6	0.08	17.5 ± 0.2	0.4 ± 0.1	3.2	3.9 ± 0.1
65	99.9776	9.9467	37.4 × 24.4	153.7	18.3	3.4 ± 0.8	8.0 ± 0.9	0.08	14.5 ± 0.2	0.8 ± 0.1	1.2	3.8 ± 0.1

Table A1: Catalog of clumps (continued).

#	Alp [J2000]	Del [J2000]	$A \times B$ [" × "]	PA [°]	Sig	$N_{H_2}^{peak}$ [Av units][a]	$N_{H_2}^{int}$ [Av units][a]	FWHM$_{dec}$[b] [pc]	T_{dust} [K]	M [$M_\odot$]	α_{BE}	$N_{H_2}^{back}$ [Av units][a]
66	99.991	9.5787	31.2 × 26.4	8.5	20.1	1.4 ± 0.3	3.0 ± 0.3	0.08	14.2 ± 0.2	0.3 ± 0.0	2.8	2.8 ± 0.1
67	99.9575	9.8404	27.4 × 21.7	145.0	15.9	1.6 ± 0.2	3.0 ± 0.2	0.06	13.9 ± 0.2	0.3 ± 0.0	2.5	2.4 ± 0.0
68	100.2132	8.9324	43.1 × 32.7	148.7	20.8	3.7 ± 0.6	14.0 ± 0.9	0.11	13.0 ± 0.2	1.4 ± 0.1	0.86	4.3 ± 0.1
69	99.9438	9.82	50.0 × 46.5	57.5	30.9	2.1 ± 0.2	14.0 ± 0.5	0.16	13.9 ± 0.2	1.5 ± 0.1	1.2	2.3 ± 0.0
70	100.3765	9.2731	54.6 × 30.9	52.7	28.4	2.7 ± 0.6	12.0 ± 0.9	0.13	13.4 ± 0.1	1.2 ± 0.1	1.2	4.0 ± 0.2
71	100.3143	9.3375	38.3 × 28.0	28.8	20.0	4 ± 1	10 ± 2	0.1	13.5 ± 0.2	1.1 ± 0.2	0.97	7.0 ± 0.4
72	100.2324	9.6418	58.2 × 39.5	15.8	21.7	6 ± 2	28 ± 4	0.16	15.1 ± 0.4	2.9 ± 0.4	0.67	8.1 ± 0.6
73*	100.4484	8.8045	34.9 × 28.7	47.8	17.4	2.1 ± 0.3	5.0 ± 0.4	0.09	13.6 ± 0.2	0.5 ± 0.0	1.9	3.5 ± 0.1
74	100.22	8.9826	30.1 × 28.7	136.3	17.6	3 ± 1	8 ± 1	0.08	13.3 ± 0.1	0.8 ± 0.1	1.1	5.4 ± 0.2
75	100.6594	9.4211	71.2 × 35.8	108.8	31.6	3.7 ± 0.8	23 ± 2	0.16	13.1 ± 0.1	2.4 ± 0.2	0.75	4.2 ± 0.3
76	100.2049	9.0746	57.5 × 31.1	105.4	19.2	4.0 ± 0.7	17 ± 1	0.13	12.5 ± 0.2	1.8 ± 0.1	0.77	5.5 ± 0.1
77	100.2746	9.5283	29.5 × 21.9	56.9	16.8	7 ± 4	13 ± 4	0.06	13.2 ± 0.1	1.3 ± 0.4	0.52	20.8 ± 0.3
78	99.9735	9.6959	33.6 × 25.5	88.5	15.4	7 ± 2	13 ± 2	0.08	13.0 ± 0.2	1.3 ± 0.2	0.67	7.7 ± 0.3
79	99.8682	9.6277	49.2 × 29.9	173.2	20.6	12 ± 4	43 ± 5	0.12	11.9 ± 0.1	4.4 ± 0.5	0.27	7.7 ± 0.8
80	100.1543	9.8742	79.4 × 50.0	161.9	36.8	9 ± 2	89 ± 4	0.21	18.5 ± 0.7	9.2 ± 0.4	0.35	5.8 ± 0.4
81	100.085	9.8963	54.0 × 27.2	71.2	18.8	2.0 ± 0.4	6.0 ± 0.5	0.12	17.7 ± 0.5	0.6 ± 0.1	2.9	4.2 ± 0.1
82	100.0651	9.4623	43.9 × 35.3	62.1	19.6	2.5 ± 0.7	10 ± 1	0.12	13.6 ± 0.2	1.1 ± 0.1	1.3	3.7 ± 0.1
83*	99.8388	9.2951	32.8 × 24.9	151.4	17.0	1.4 ± 0.4	3.0 ± 0.5	0.08	13.8 ± 0.2	0.3 ± 0.1	2.7	2.9 ± 0.0
84	100.5825	9.0739	50.9 × 31.0	162.1	19.2	4 ± 1	16 ± 2	0.12	12.3 ± 0.1	1.6 ± 0.2	0.79	5.9 ± 0.1
85	100.0642	9.4975	55.7 × 32.6	69.7	20.0	3.0 ± 0.4	14.0 ± 0.7	0.14	13.6 ± 0.2	1.4 ± 0.1	1.1	3.9 ± 0.1
86	100.1978	9.7694	35.2 × 35.1	24.4	18.8	1.9 ± 0.7	6 ± 1	0.11	22.0 ± 0.5	0.7 ± 0.1	3.0	4.8 ± 0.2
87	99.9733	9.706	30.7 × 26.9	48.4	14.7	7 ± 3	14 ± 3	0.08	12.9 ± 0.2	1.4 ± 0.3	0.59	8.2 ± 0.3
88	100.1362	9.886	39.5 × 26.6	15.5	16.8	6 ± 2	14 ± 2	0.09	17.7 ± 0.7	1.5 ± 0.2	0.92	6.5 ± 0.4
89	100.3631	9.3662	32.6 × 26.1	175.5	12.0	11 ± 2	18 ± 2	0.08	12.6 ± 0.1	1.8 ± 0.2	0.46	11.6 ± 0.6
90	100.5747	9.0	33.8 × 25.5	74.7	14.3	3.0 ± 0.9	6 ± 1	0.08	12.5 ± 0.1	0.6 ± 0.1	1.4	5.4 ± 0.2
91	100.2115	9.5879	38.6 × 34.9	27.1	13.7	19 ± 7	51 ± 8	0.11	12.9 ± 0.2	5.2 ± 0.8	0.23	20 ± 1
92	100.1875	9.6607	39.5 × 36.2	112.1	13.0	3 ± 1	10 ± 2	0.12	16.8 ± 0.3	1.0 ± 0.2	1.6	5.6 ± 0.2
93	100.0378	9.7167	66.5 × 48.9	95.0	29.8	4 ± 1	30 ± 2	0.19	15.0 ± 0.4	3.1 ± 0.2	0.76	3.9 ± 0.1
94	100.1673	9.7977	38.5 × 33.2	19.4	20.2	1.7 ± 0.5	6.0 ± 0.8	0.11	20.6 ± 0.2	0.6 ± 0.1	3.0	3.4 ± 0.1
95	100.2196	8.9951	64.8 × 34.5	150.7	19.5	4.3 ± 0.9	22 ± 2	0.15	13.1 ± 0.1	2.3 ± 0.2	0.72	6.0 ± 0.2
96	100.6249	9.0262	48.3 × 35.3	63.9	21.1	2.9 ± 0.4	13.0 ± 0.6	0.13	12.8 ± 0.1	1.3 ± 0.1	1.0	4.3 ± 0.0
97	100.5551	8.9896	25.9 × 24.6	164.2	13.3	2 ± 1	3 ± 1	0.06	13.3 ± 0.3	0.4 ± 0.1	1.7	5.1 ± 0.2
98	100.7344	9.3178	69.8 × 39.3	175.9	27.8	3.5 ± 0.4	25.0 ± 0.8	0.17	13.1 ± 0.1	2.6 ± 0.1	0.72	4.0 ± 0.1
99	100.3448	9.3903	59.3 × 44.4	116.7	20.2	8 ± 3	51 ± 5	0.17	13.5 ± 0.1	5.3 ± 0.5	0.35	13.6 ± 0.6
100	100.096	9.8506	42.0 × 34.8	162.8	20.8	3 ± 1	10 ± 2	0.12	19.0 ± 0.4	1.0 ± 0.2	1.9	4.4 ± 0.4
101	100.2797	8.9593	39.6 × 25.9	17.2	14.6	1.7 ± 0.4	4.0 ± 0.5	0.09	13.6 ± 0.1	0.4 ± 0.1	2.5	3.8 ± 0.1
102	100.1655	8.9167	33.1 × 30.1	76.7	16.0	2.8 ± 0.9	8 ± 1	0.09	13.2 ± 0.1	0.8 ± 0.1	1.2	5.0 ± 0.2
103	100.2451	9.5575	32.0 × 25.2	151.1	13.8	7 ± 5	12 ± 6	0.08	14.2 ± 0.2	1.2 ± 0.6	0.75	18 ± 1
104	100.1744	9.7514	73.3 × 56.5	101.7	32.5	2.6 ± 0.6	27 ± 2	0.22	21.2 ± 0.8	2.8 ± 0.2	1.4	3.6 ± 0.2
105	100.2541	9.3378	65.8 × 42.6	179.1	19.8	2.9 ± 0.6	18 ± 1	0.17	13.5 ± 0.2	1.9 ± 0.1	1.0	4.6 ± 0.1
106	100.2503	9.59	37.3 × 29.1	125.1	13.9	45 ± 11	114 ± 12	0.1	14.8 ± 0.5	12 ± 1	0.1	44.1 ± 0.6
107	100.0727	9.4603	31.7 × 24.6	129.4	9.9	1.9 ± 0.8	4.0 ± 0.9	0.07	13.5 ± 0.1	0.4 ± 0.1	2.0	4.0 ± 0.2
108*	100.434	8.8942	28.9 × 23.4	103.2	14.4	1.4 ± 0.5	3.0 ± 0.6	0.06	13.5 ± 0.2	0.3 ± 0.1	2.6	3.0 ± 0.1
109	100.2467	9.0244	63.2 × 35.1	172.2	21.4	4 ± 1	16 ± 2	0.15	12.5 ± 0.2	1.7 ± 0.2	0.93	6.7 ± 0.7
110	100.0598	9.213	34.0 × 24.7	154.0	15.3	1.7 ± 0.3	4.0 ± 0.4	0.08	13.4 ± 0.1	0.4 ± 0.0	2.1	5.0 ± 0.1
111	100.2915	9.9672	29.9 × 25.9	42.8	14.5	2.3 ± 0.9	5 ± 1	0.07	13.3 ± 0.1	0.5 ± 0.1	1.6	6.2 ± 0.1
112	100.094	9.9152	23.7 × 23.7	149.1	13.4	1.7 ± 0.6	3.0 ± 0.7	0.05	16.4 ± 0.2	0.3 ± 0.1	2.5	4.4 ± 0.0
113	100.1795	9.1332	35.3 × 30.0	20.3	14.0	2.7 ± 0.8	7 ± 1	0.09	13.2 ± 0.1	0.8 ± 0.1	1.3	6.7 ± 0.0
114	100.1754	9.1555	37.9 × 29.6	32.7	14.2	3 ± 1	8 ± 1	0.1	13.0 ± 0.1	0.8 ± 0.1	1.3	6.5 ± 0.2
115	100.2806	9.7276	50.4 × 35.6	53.6	12.1	3 ± 2	10 ± 3	0.13	14.6 ± 0.1	1.0 ± 0.3	1.6	8.8 ± 0.4
116	100.1912	9.6705	67.9 × 49.3	133.8	24.3	3 ± 1	29 ± 3	0.19	17.2 ± 0.5	3.1 ± 0.3	0.88	4.8 ± 0.3
117	99.9587	9.9553	37.3 × 28.3	138.8	13.7	2.9 ± 0.9	7 ± 1	0.09	15.7 ± 0.2	0.8 ± 0.1	1.5	4.0 ± 0.2
118	100.4639	9.2354	54.6 × 41.8	155.9	21.4	1.9 ± 0.9	11 ± 2	0.16	13.5 ± 0.1	1.1 ± 0.2	1.6	4.8 ± 0.1
119	100.7421	9.4783	44.0 × 31.9	47.3	18.3	1.2 ± 0.1	5.0 ± 0.2	0.11	14.3 ± 0.2	0.5 ± 0.0	2.7	2.3 ± 0.0
120	100.4643	9.4295	46.0 × 42.1	11.5	24.5	2.5 ± 0.6	14 ± 1	0.14	13.7 ± 0.2	1.4 ± 0.1	1.1	4.2 ± 0.2
121	100.1103	9.5779	40.7 × 31.8	0.8	13.9	2.6 ± 0.8	8 ± 1	0.11	15.0 ± 0.1	0.9 ± 0.1	1.5	7.2 ± 0.1
122	100.1735	9.8958	30.9 × 23.3	93.5	13.3	1.1 ± 0.5	2.0 ± 0.5	0.07	17.7 ± 0.2	0.2 ± 0.1	5.3	3.8 ± 0.1
123	100.3207	9.7433	49.9 × 42.8	35.8	20.8	4 ± 2	20 ± 3	0.15	14.5 ± 0.1	2.1 ± 0.3	0.85	6.9 ± 0.5
124	100.642	9.5663	33.6 × 27.6	56.7	14.1	1.5 ± 0.4	4.0 ± 0.5	0.09	13.8 ± 0.1	0.4 ± 0.1	2.5	3.2 ± 0.1
125	100.2854	9.5877	33.2 × 27.5	52.6	12.5	23 ± 13	49 ± 14	0.08	13.4 ± 0.3	5 ± 1	0.18	51 ± 2
126	100.1556	9.8406	44.1 × 34.0	15.8	12.6	2 ± 1	7 ± 2	0.12	18.5 ± 0.4	0.7 ± 0.2	2.6	4.2 ± 0.3
127	100.4369	8.8042	39.6 × 28.4	19.0	12.9	1.8 ± 0.2	4.0 ± 0.3	0.1	13.6 ± 0.2	0.4 ± 0.0	2.5	3.4 ± 0.0
128*	100.3264	9.3515	37.5 × 28.1	42.0	12.1	5 ± 2	11 ± 2	0.09	13.5 ± 0.2	1.2 ± 0.2	0.88	9.8 ± 0.5
129	100.1184	9.8625	59.1 × 37.7	96.4	13.4	4 ± 1	21 ± 2	0.15	19.7 ± 0.5	2.1 ± 0.2	1.2	5.6 ± 0.3

Table A1: Catalog of clumps (continued).

#	Alp [J2000]	Del [J2000]	$A \times B$ ["$\times$"]	PA [°]	Sig	$N_{H_2}^{peak}$ [Av units]^a	$N_{H_2}^{int}$ [Av units]^a	FWHM$_{dec}$ ^{b} [pc]	T_{dust} [K]	M [$M_\odot$]	α_{BE}	$N_{H_2}^{back}$ [Av units]^a
130	100.4482	8.792	45.3 × 30.7	173.2	14.2	1.7 ± 0.3	6.0 ± 0.4	0.11	13.6 ± 0.2	0.6 ± 0.1	2.3	3.1 ± 0.1
131*	100.1699	8.9387	43.1 × 25.1	53.0	14.0	2.7 ± 0.5	8.0 ± 0.8	0.1	13.1 ± 0.1	0.8 ± 0.1	1.3	6.3 ± 0.2
132	100.583	9.415	29.9 × 24.0	73.2	11.9	1.7 ± 0.8	3.0 ± 0.9	0.07	13.4 ± 0.1	0.3 ± 0.1	2.5	4.9 ± 0.2
133	100.0878	9.2379	70.8 × 41.2	29.5	20.6	2.2 ± 0.5	16 ± 1	0.18	13.6 ± 0.1	1.7 ± 0.1	1.2	4.5 ± 0.0
134	100.2048	9.4749	34.9 × 24.6	19.8	12.4	1.7 ± 0.6	4.0 ± 0.7	0.08	14.9 ± 0.1	0.4 ± 0.1	2.6	5.6 ± 0.1
135	100.3867	9.7979	40.7 × 38.9	67.4	15.3	1.5 ± 0.3	6.0 ± 0.4	0.12	15.1 ± 0.2	0.6 ± 0.0	2.5	2.9 ± 0.1
136	100.436	9.2739	42.4 × 25.8	79.5	13.3	1.6 ± 0.4	5.0 ± 0.6	0.1	14.0 ± 0.1	0.5 ± 0.1	2.3	4.0 ± 0.1
137	100.2108	9.6019	28.3 × 25.4	72.3	12.2	8 ± 3	16 ± 3	0.07	13.5 ± 0.2	1.7 ± 0.3	0.45	15.7 ± 0.5
138	100.09	9.5957	33.9 × 24.3	174.1	13.1	1.7 ± 0.6	4.0 ± 0.7	0.08	15.8 ± 0.1	0.4 ± 0.1	2.7	5.5 ± 0.1
139	100.0368	9.6407	24.3 × 24.2	47.6	11.4	2.4 ± 0.6	3.0 ± 0.6	0.06	16.1 ± 0.2	0.4 ± 0.1	2.1	5.9 ± 0.0
140	99.9155	9.5519	53.3 × 34.0	22.3	14.3	6 ± 2	24 ± 2	0.13	12.8 ± 0.2	2.5 ± 0.2	0.57	4.0 ± 0.4
141	100.1577	9.0647	64.2 × 36.4	154.7	15.8	3 ± 1	14 ± 2	0.16	12.6 ± 0.2	1.5 ± 0.2	1.1	5.4 ± 0.2
142	100.0998	9.1946	46.0 × 34.1	103.0	16.3	1.7 ± 0.6	8 ± 1	0.12	13.6 ± 0.1	0.8 ± 0.1	1.7	4.1 ± 0.1
143	100.2731	9.6803	39.9 × 29.9	127.7	12.9	3 ± 1	9 ± 2	0.1	14.5 ± 0.2	0.9 ± 0.2	1.4	7.3 ± 0.4
144	100.4178	9.8553	61.1 × 44.9	46.0	18.3	1.6 ± 0.2	11.0 ± 0.4	0.17	13.8 ± 0.2	1.2 ± 0.0	1.7	2.7 ± 0.0
145	100.2594	9.8615	38.6 × 32.2	159.2	13.2	1.6 ± 0.8	5 ± 1	0.11	15.9 ± 0.2	0.5 ± 0.1	2.8	6.1 ± 0.3
146	100.0022	9.1453	81.3 × 49.2	8.8	20.2	2.6 ± 0.7	25 ± 2	0.21	13.8 ± 0.1	2.5 ± 0.2	0.97	4.0 ± 0.2
147	100.3188	9.3958	45.5 × 31.7	171.5	11.9	9 ± 2	28 ± 3	0.12	14.2 ± 0.2	2.9 ± 0.3	0.0	16.9 ± 0.6
148	100.2951	9.5625	29.1 × 23.3	2.6	11.4	13 ± 6	22 ± 7	0.07	12.6 ± 0.2	2.2 ± 0.7	0.31	27.4 ± 0.3
149	100.1934	9.6148	37.1 × 29.3	167.1	11.4	5 ± 2	13 ± 2	0.1	14.5 ± 0.2	1.4 ± 0.2	0.83	10.6 ± 0.3
150	100.2077	9.7861	46.5 × 34.8	43.1	14.7	1.7 ± 0.7	7 ± 1	0.13	21.6 ± 0.5	0.8 ± 0.1	2.8	5.1 ± 0.1
151	100.0163	9.9338	31.8 × 30.7	77.5	13.0	1.3 ± 0.3	4.0 ± 0.4	0.09	16.0 ± 0.1	0.4 ± 0.1	3.1	3.5 ± 0.1
152	100.6882	9.3968	39.1 × 34.3	31.1	15.7	1.4 ± 0.6	5 ± 1	0.11	13.4 ± 0.1	0.5 ± 0.1	2.6	2.9 ± 0.1
153	100.5352	9.6892	24.5 × 23.1	25.0	11.5	0.6 ± 0.2	1.0 ± 0.2	0.05	15.0 ± 0.1	0.1 ± 0.0	6.1	2.5 ± 0.0
154	99.7937	9.7389	31.5 × 26.2	73.7	11.6	1.2 ± 0.1	2.0 ± 0.1	0.08	14.3 ± 0.1	0.2 ± 0.0	5.4	2.3 ± 0.1
155	100.5735	8.9423	35.2 × 30.5	162.6	10.3	3.1 ± 0.7	9 ± 1	0.1	12.7 ± 0.1	1.0 ± 0.1	1.0	4.8 ± 0.2
156	100.1781	8.9031	31.2 × 29.2	138.6	12.5	1.7 ± 0.7	4 ± 1	0.08	13.5 ± 0.1	0.4 ± 0.1	2.4	3.9 ± 0.2
157	100.398	9.5311	33.2 × 24.1	30.6	10.8	1.6 ± 0.4	3.0 ± 0.4	0.08	13.9 ± 0.1	0.3 ± 0.0	2.7	4.1 ± 0.0
158	100.1566	9.7885	50.2 × 32.7	149.7	13.0	1.4 ± 0.4	5.0 ± 0.5	0.13	20.2 ± 0.2	0.6 ± 0.1	3.9	3.8 ± 0.1
159	100.3769	8.8673	56.4 × 33.4	92.8	13.2	2.0 ± 0.4	8.0 ± 0.6	0.14	13.7 ± 0.1	0.8 ± 0.1	1.9	3.7 ± 0.0
160*	100.5798	9.03	36.2 × 26.0	14.2	12.1	1.9 ± 0.7	5.0 ± 0.9	0.09	12.9 ± 0.2	0.5 ± 0.1	1.8	4.3 ± 0.1
161	100.467	9.1946	35.8 × 23.0	66.2	12.4	1.1 ± 0.6	3.0 ± 0.8	0.08	13.9 ± 0.1	0.3 ± 0.1	3.4	3.6 ± 0.1
162	100.5067	9.4543	39.9 × 32.4	59.8	13.2	1.1 ± 0.2	4.0 ± 0.3	0.11	13.9 ± 0.1	0.4 ± 0.0	3.0	2.5 ± 0.0
163	100.2866	9.4104	26.2 × 23.0	27.2	11.1	4 ± 2	7 ± 2	0.06	16.4 ± 0.3	0.7 ± 0.2	1.1	9.8 ± 0.3
164	100.2973	9.5064	34.1 × 25.5	17.6	10.8	28 ± 7	50 ± 7	0.08	14.1 ± 0.7	5.2 ± 0.8	0.18	44 ± 3
165	100.1823	9.0229	68.1 × 57.3	99.1	14.6	2 ± 1	23 ± 3	0.21	13.1 ± 0.1	2.4 ± 0.3	0.95	5.6 ± 0.5
166	100.1345	9.127	71.8 × 60.0	3.2	20.6	3.4 ± 0.9	39 ± 2	0.22	13.3 ± 0.1	4.0 ± 0.3	0.61	5.0 ± 0.2
167	100.3678	9.5892	27.1 × 23.7	50.0	10.1	3.2 ± 0.6	5.0 ± 0.6	0.06	14.6 ± 0.2	0.5 ± 0.1	1.4	5.6 ± 0.0
168	100.1722	9.9264	42.3 × 34.0	106.6	12.4	1.1 ± 0.4	4.0 ± 0.7	0.12	16.7 ± 0.1	0.4 ± 0.1	3.7	3.4 ± 0.1
169	100.3882	9.325	36.5 × 31.0	31.4	10.8	2 ± 1	6 ± 1	0.1	13.4 ± 0.1	0.6 ± 0.1	1.8	7.1 ± 0.1
170	100.2085	9.6972	35.8 × 24.6	49.7	10.8	1.2 ± 0.5	3.0 ± 0.6	0.08	17.5 ± 0.2	0.3 ± 0.1	4.4	3.9 ± 0.1
171	100.1884	9.8296	41.4 × 32.7	64.5	15.5	0.8 ± 0.2	3.0 ± 0.3	0.11	18.8 ± 0.4	0.3 ± 0.0	5.6	2.8 ± 0.0
172	99.8817	9.6786	27.6 × 24.2	165.0	10.9	1.2 ± 0.3	2.0 ± 0.4	0.06	13.8 ± 0.1	0.2 ± 0.0	3.3	4.0 ± 0.0
173	100.5193	8.8943	32.0 × 24.2	139.5	10.9	1.3 ± 0.3	3.0 ± 0.4	0.07	13.5 ± 0.2	0.3 ± 0.0	2.9	2.8 ± 0.0
174*	100.111	8.9833	57.2 × 32.3	44.0	13.6	2.1 ± 0.8	9 ± 1	0.14	13.3 ± 0.1	0.9 ± 0.1	1.7	4.1 ± 0.2
175	100.4885	9.5556	74.0 × 45.2	52.5	13.8	1.1 ± 0.2	9.0 ± 0.5	0.19	14.0 ± 0.2	0.9 ± 0.1	2.4	2.6 ± 0.1
176	99.9884	9.3223	34.1 × 31.4	143.5	10.7	1.4 ± 0.2	4.0 ± 0.3	0.1	13.4 ± 0.1	0.4 ± 0.0	2.6	3.6 ± 0.0
177	100.2578	9.5549	33.4 × 27.7	82.4	10.1	14 ± 9	30 ± 9	0.09	12.7 ± 0.1	3.1 ± 0.9	0.29	33 ± 4
178	99.9995	9.3985	42.9 × 41.9	123.5	15.6	1.3 ± 0.2	7.0 ± 0.3	0.13	13.8 ± 0.1	0.7 ± 0.0	2.2	2.5 ± 0.0
179	100.2595	9.7602	55.4 × 33.0	160.7	12.0	1.6 ± 0.6	6 ± 1	0.14	15.4 ± 0.2	0.7 ± 0.1	2.6	7.0 ± 0.1
180	100.2866	9.0061	40.1 × 30.9	24.0	11.7	1.9 ± 0.8	6 ± 1	0.11	13.5 ± 0.1	0.6 ± 0.1	2.0	4.6 ± 0.2
181	100.113	9.1433	56.7 × 49.6	12.3	13.7	1.8 ± 0.6	12 ± 1	0.17	13.6 ± 0.1	1.3 ± 0.1	1.5	4.7 ± 0.1
182	100.4264	9.4137	72.1 × 34.7	16.4	13.3	1.0 ± 0.4	5.0 ± 0.7	0.16	15.1 ± 0.1	0.6 ± 0.1	3.7	4.1 ± 0.1
183	100.1023	9.5246	47.2 × 35.8	48.0	12.3	1.2 ± 0.4	5.0 ± 0.6	0.13	14.4 ± 0.2	0.5 ± 0.1	3.3	4.0 ± 0.1
184	100.2541	9.656	34.5 × 30.1	30.6	14.3	2 ± 1	6 ± 1	0.09	15.5 ± 0.1	0.6 ± 0.1	2.0	7.1 ± 0.2
185	100.5251	9.1592	53.8 × 41.0	54.7	12.1	7 ± 2	37 ± 3	0.15	12.3 ± 0.3	3.8 ± 0.3	0.41	10.0 ± 0.7
186	100.7216	9.2688	48.9 × 39.1	123.7	13.3	2.1 ± 0.6	10 ± 1	0.14	13.5 ± 0.1	1.1 ± 0.1	1.4	3.6 ± 0.1
187	100.6924	9.3673	37.0 × 33.5	51.6	12.1	1.4 ± 0.5	5.0 ± 0.8	0.11	13.4 ± 0.1	0.5 ± 0.1	2.5	4.0 ± 0.0
188	100.4766	9.4058	44.4 × 33.3	122.5	11.4	1.3 ± 0.5	5.0 ± 0.8	0.12	14.6 ± 0.1	0.5 ± 0.1	2.9	3.6 ± 0.1
189	100.0175	9.6433	35.3 × 33.8	84.8	10.7	1.4 ± 0.5	4.0 ± 0.7	0.1	15.8 ± 0.1	0.4 ± 0.1	3.5	5.2 ± 0.2
190	100.4665	8.9984	31.6 × 23.2	128.7	10.6	1.0 ± 0.2	2.0 ± 0.3	0.07	13.7 ± 0.1	0.2 ± 0.0	3.5	3.0 ± 0.0
191	100.2866	8.9851	42.1 × 30.4	51.5	11.3	1.8 ± 0.6	6.0 ± 0.8	0.11	13.8 ± 0.1	0.6 ± 0.1	2.1	4.0 ± 0.1
192	100.332	9.3187	53.7 × 29.8	85.9	12.4	1.8 ± 0.9	6 ± 1	0.12	14.4 ± 0.1	0.7 ± 0.1	2.1	5.3 ± 0.2
193	100.0675	9.1705	28.1 × 22.7	166.9	9.8	1.4 ± 0.4	2.0 ± 0.5	0.06	13.4 ± 0.1	0.2 ± 0.1	3.1	5.1 ± 0.0
194	100.307	9.4094	56.4 × 31.8	26.6	9.7	23 ± 3	83 ± 5	0.13	13.8 ± 0.3	8.6 ± 0.5	0.18	18 ± 1
195	100.1469	9.5938	43.4 × 40.0	40.8	12.9	3 ± 1	14 ± 3	0.13	16.7 ± 0.3	1.5 ± 0.3	1.2	7.1 ± 0.3

Table A1: Catalog of clumps (continued).

#	Alp [J2000]	Del [J2000]	$A \times B$ ["$\times$"]	PA [°]	Sig	$N_{H_2}^{peak}$ [Av units][a]	$N_{H_2}^{int}$ [Av units][a]	$FWHM_{dec}$[b] [pc]	T_{dust} [K]	M [$M_\odot$]	α_{BE}	$N_{H_2}^{back}$ [Av units][a]
196	100.3293	9.8023	47.4×28.1	140.5	11.3	1 ± 1	3 ± 1	0.11	14.8 ± 0.2	0.3 ± 0.1	4.5	5.4 ± 0.4
197	100.0306	9.9795	46.5×38.3	161.4	11.9	2.3 ± 0.4	10.0 ± 0.6	0.13	15.8 ± 0.2	1.0 ± 0.1	1.7	2.9 ± 0.1
198	100.5287	9.2781	52.4×39.1	18.0	14.0	2.0 ± 0.6	10 ± 1	0.15	13.6 ± 0.1	1.1 ± 0.1	1.5	4.0 ± 0.1
199	100.4731	9.3384	37.7×25.7	38.9	9.9	1.7 ± 0.3	4.0 ± 0.3	0.09	14.3 ± 0.1	0.4 ± 0.0	2.7	4.6 ± 0.2
200	100.4175	9.4934	39.8×27.9	9.9	10.2	1.7 ± 0.5	4.0 ± 0.6	0.1	14.2 ± 0.2	0.4 ± 0.1	2.6	4.1 ± 0.0
201	100.5678	9.6361	37.4×23.9	15.1	10.0	0.7 ± 0.2	1.0 ± 0.3	0.08	14.3 ± 0.1	0.1 ± 0.0	7.0	2.7 ± 0.0
202	100.1883	9.5249	48.1×29.7	173.9	10.2	2.9 ± 0.7	9.0 ± 0.9	0.12	15.0 ± 0.1	0.9 ± 0.1	1.5	6.5 ± 0.1
203	100.2228	9.6119	43.5×28.1	7.9	9.7	20 ± 6	57 ± 7	0.1	12.9 ± 0.2	5.9 ± 0.7	0.19	19 ± 2
204	100.6019	8.9422	34.6×31.9	12.9	11.5	1.9 ± 0.6	6.0 ± 0.9	0.1	13.1 ± 0.1	0.6 ± 0.1	1.8	4.5 ± 0.1
205	100.3301	9.6818	56.2×34.8	43.8	12.3	4 ± 2	17 ± 3	0.14	14.5 ± 0.1	1.7 ± 0.3	1.0	7.7 ± 0.6
206	100.1509	9.8352	61.0×36.1	178.2	11.7	1 ± 1	6 ± 2	0.15	18.3 ± 0.4	0.7 ± 0.2	3.3	4.3 ± 0.3
207	100.0777	9.8355	33.5×22.9	171.4	10.2	1.1 ± 0.7	2.0 ± 0.8	0.07	18.4 ± 0.2	0.2 ± 0.1	5.3	4.2 ± 0.2
208	100.393	8.7956	27.3×22.9	61.5	9.9	0.8 ± 0.2	1.0 ± 0.3	0.06	13.9 ± 0.1	0.1 ± 0.0	4.9	3.0 ± 0.0
209	100.6358	9.2201	41.5×28.3	121.7	10.3	1.1 ± 0.4	3.0 ± 0.5	0.1	13.8 ± 0.1	0.3 ± 0.1	3.9	4.3 ± 0.1
210*	100.1728	9.0687	52.5×36.9	37.7	10.6	1.8 ± 0.8	7 ± 1	0.14	12.7 ± 0.1	0.7 ± 0.1	2.1	6.8 ± 0.2
211	99.8251	9.6745	39.1×26.2	141.1	11.2	0.8 ± 0.3	2.0 ± 0.5	0.09	14.3 ± 0.1	0.2 ± 0.1	4.8	2.5 ± 0.1
212	100.4328	9.4874	56.5×46.5	116.7	13.3	2.1 ± 0.4	13.0 ± 0.7	0.17	14.2 ± 0.1	1.3 ± 0.1	1.5	4.0 ± 0.1
213	100.1546	9.1013	50.2×30.6	122.3	10.7	1.8 ± 0.8	6 ± 1	0.12	12.8 ± 0.1	0.6 ± 0.1	2.2	6.7 ± 0.4
214	99.8508	9.513	49.7×39.1	4.2	18.1	0.8 ± 0.2	4.0 ± 0.3	0.14	14.1 ± 0.1	0.4 ± 0.0	3.8	1.7 ± 0.0
215	100.2164	9.9611	51.6×29.7	47.7	11.0	1.3 ± 0.5	5.0 ± 0.8	0.12	16.5 ± 0.1	0.5 ± 0.1	3.5	3.8 ± 0.1
216	100.1868	9.5419	36.1×31.9	29.6	10.9	2 ± 1	7 ± 2	0.1	15.1 ± 0.1	0.7 ± 0.2	1.8	8.2 ± 0.5
217	100.393	9.7742	67.7×65.9	157.0	19.8	1.9 ± 0.4	21.0 ± 0.9	0.22	14.5 ± 0.2	2.1 ± 0.1	1.3	3.2 ± 0.1
218	100.3331	9.4513	38.3×32.5	39.8	10.5	5 ± 2	15 ± 3	0.11	14.2 ± 0.2	1.5 ± 0.3	0.83	14.1 ± 0.6
219	100.0169	9.3053	35.0×26.9	26.4	9.8	1.2 ± 0.3	3.0 ± 0.4	0.09	13.4 ± 0.1	0.3 ± 0.0	3.0	3.8 ± 0.1
220	100.0327	9.9133	34.0×27.6	144.4	9.8	1.1 ± 0.3	3.0 ± 0.4	0.09	16.9 ± 0.2	0.3 ± 0.0	4.7	3.3 ± 0.1
221	100.2234	9.4137	35.1×29.0	101.4	9.7	0.8 ± 0.4	2.0 ± 0.6	0.09	14.8 ± 0.1	0.3 ± 0.1	4.5	3.7 ± 0.1
222	100.1727	9.2276	39.8×33.6	23.4	10.6	1.1 ± 0.3	4.0 ± 0.5	0.11	13.9 ± 0.1	0.4 ± 0.1	3.1	4.1 ± 0.0
223	100.0034	9.3185	48.9×39.3	142.6	10.5	1.8 ± 0.4	8.0 ± 0.6	0.14	13.4 ± 0.1	0.8 ± 0.1	1.9	3.5 ± 0.1
224	99.9801	9.3956	41.0×32.4	177.0	11.2	1.1 ± 0.2	4.0 ± 0.4	0.11	13.7 ± 0.1	0.4 ± 0.0	3.1	2.6 ± 0.0
225	100.168	8.8929	38.3×26.7	23.5	9.4	2.9 ± 0.7	7.0 ± 0.8	0.09	13.3 ± 0.1	0.7 ± 0.1	1.5	4.3 ± 0.1
226	100.1345	9.7806	38.2×29.7	13.0	9.5	0.9 ± 0.6	2.0 ± 0.7	0.1	20.0 ± 0.1	0.2 ± 0.1	7.5	3.6 ± 0.1
227	100.1679	8.9551	35.4×26.7	22.8	9.5	1.9 ± 0.6	5.0 ± 0.8	0.09	13.1 ± 0.1	0.5 ± 0.1	1.9	6.0 ± 0.1
228	100.2744	9.4879	52.5×34.8	29.2	9.8	32 ± 10	130 ± 15	0.14	14.4 ± 0.6	13 ± 2	0.12	28 ± 4
229	100.4712	9.7146	44.5×31.1	101.7	10.8	0.8 ± 0.3	3.0 ± 0.5	0.11	14.4 ± 0.1	0.3 ± 0.1	4.5	2.8 ± 0.1
230	100.5055	9.0346	40.9×24.4	13.9	9.4	1.3 ± 0.2	3.0 ± 0.3	0.09	13.6 ± 0.1	0.3 ± 0.0	3.0	3.5 ± 0.1
231	100.6787	9.2856	50.0×33.1	9.4	10.6	1.5 ± 0.4	6.0 ± 0.6	0.13	13.7 ± 0.1	0.6 ± 0.1	2.4	3.6 ± 0.1
232	100.2841	9.8799	54.2×47.1	104.2	13.7	1.7 ± 0.8	11 ± 2	0.17	15.0 ± 0.1	1.1 ± 0.2	1.9	6.6 ± 0.2
233	100.0403	9.8045	48.1×35.8	45.5	11.7	0.6 ± 0.3	3.0 ± 0.5	0.13	16.9 ± 0.3	0.3 ± 0.1	6.8	2.7 ± 0.1
234	99.8508	9.4494	22.7×20.4	94.0	10.1	0.5 ± 0.1	1.0 ± 0.1	0.04	14.0 ± 0.1	0.1 ± 0.0	6.1	1.8 ± 0.0
235	100.5251	9.1855	39.1×30.7	109.6	9.5	3 ± 1	9 ± 2	0.1	12.4 ± 0.1	0.9 ± 0.2	1.2	12.0 ± 0.3
236	100.6078	9.7215	59.5×39.0	90.2	11.8	1.1 ± 0.2	6.0 ± 0.3	0.16	15.6 ± 0.3	0.6 ± 0.0	3.2	2.1 ± 0.0
237	100.3463	9.6186	41.9×31.3	134.1	10.1	0.9 ± 0.5	3.0 ± 0.8	0.11	15.2 ± 0.1	0.3 ± 0.1	4.8	4.6 ± 0.2
238	99.914	9.7416	50.2×30.3	3.4	11.8	0.8 ± 0.3	4.0 ± 0.6	0.12	14.6 ± 0.1	0.4 ± 0.1	4.0	3.1 ± 0.1
239	100.4243	8.8565	53.8×41.1	16.7	10.8	1.3 ± 0.3	7.0 ± 0.6	0.15	13.6 ± 0.1	0.8 ± 0.1	2.3	3.5 ± 0.1
240	100.1624	10.0982	43.0×31.3	169.2	9.9	0.9 ± 0.2	3.0 ± 0.3	0.11	14.4 ± 0.2	0.3 ± 0.0	4.4	2.5 ± 0.1
241	99.9246	9.6363	36.2×28.7	71.0	9.2	0.9 ± 0.3	2.0 ± 0.4	0.09	14.5 ± 0.1	0.3 ± 0.1	4.5	3.7 ± 0.0
242	100.3002	9.5817	40.1×33.1	170.4	9.5	16 ± 8	49 ± 10	0.11	12.7 ± 0.3	5 ± 1	0.23	33 ± 3
243*	100.0288	9.5179	34.4×23.7	45.1	9.4	0.9 ± 0.4	2.0 ± 0.5	0.08	14.1 ± 0.1	0.2 ± 0.1	4.3	3.6 ± 0.1
244	100.2381	9.8821	45.9×40.7	41.0	9.7	1.3 ± 0.8	6 ± 1	0.14	16.9 ± 0.4	0.6 ± 0.1	3.2	5.1 ± 0.2
245	100.1924	10.1409	50.3×31.8	90.7	9.7	1.1 ± 0.2	4.0 ± 0.3	0.13	14.6 ± 0.2	0.4 ± 0.0	3.9	2.7 ± 0.1
246	100.5613	9.1736	33.2×31.1	69.7	9.3	1.7 ± 0.9	5 ± 1	0.09	13.5 ± 0.1	0.5 ± 0.1	2.1	5.2 ± 0.3
247	100.6046	9.3906	33.4×25.8	10.3	9.3	1.0 ± 0.5	2.0 ± 0.6	0.08	13.9 ± 0.1	0.2 ± 0.1	3.9	4.7 ± 0.0
248	100.3279	9.1959	37.9×28.7	179.6	9.2	0.6 ± 0.1	2.0 ± 0.2	0.1	14.4 ± 0.1	0.2 ± 0.0	6.4	2.8 ± 0.0
249	100.2868	9.733	60.7×49.7	170.2	11.1	3 ± 1	24 ± 3	0.18	14.5 ± 0.1	2.5 ± 0.4	0.87	9.1 ± 0.5
250	100.1913	9.8507	37.9×35.2	160.4	9.2	0.6 ± 0.2	2.0 ± 0.3	0.11	18.8 ± 0.3	0.2 ± 0.0	8.2	2.8 ± 0.0
251	100.105	10.0504	45.9×34.5	129.2	9.1	0.7 ± 0.2	3.0 ± 0.3	0.12	15.1 ± 0.1	0.3 ± 0.0	6.0	2.1 ± 0.0
252	100.0991	9.6237	46.2×36.4	22.1	9.2	1.1 ± 0.6	5 ± 1	0.13	16.0 ± 0.1	0.5 ± 0.1	3.4	5.6 ± 0.1
253	100.1044	9.9756	63.1×44.1	111.7	10.3	1.0 ± 0.4	6.0 ± 0.8	0.17	15.0 ± 0.2	0.6 ± 0.1	3.4	2.4 ± 0.2
254	100.2719	9.4106	51.3×42.5	30.8	9.2	3 ± 2	14 ± 3	0.15	14.2 ± 0.1	1.5 ± 0.3	1.2	7.8 ± 0.4
255	100.0803	9.5105	57.3×48.6	154.0	9.5	2.3 ± 0.6	15 ± 1	0.17	14.0 ± 0.1	1.6 ± 0.1	1.3	4.0 ± 0.2
256	99.8548	9.8456	50.9×37.3	128.7	9.5	0.7 ± 0.1	3.0 ± 0.3	0.14	14.5 ± 0.1	0.3 ± 0.0	4.8	2.1 ± 0.0

[a] 1 Av = 10^{21} H$_2$ cm^{-2}
[b] source deconvolved size at FWHM, $FWHM_{dec} = (A \times B - 18.2^2)^{1/2}$, minimized at half the beam size
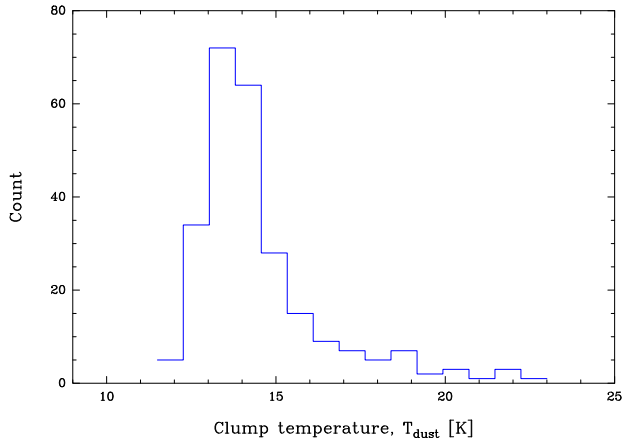* Clumps located outside the area where YSOs have been detected, excluded in the *nnd* analysis.

Fig. A4: Temperature distribution of the 256 clumps detected in NGC 2264. The temperature dispersion between clumps in small, 80% of the clumps having a temperature between 12.7 and 16.9 K
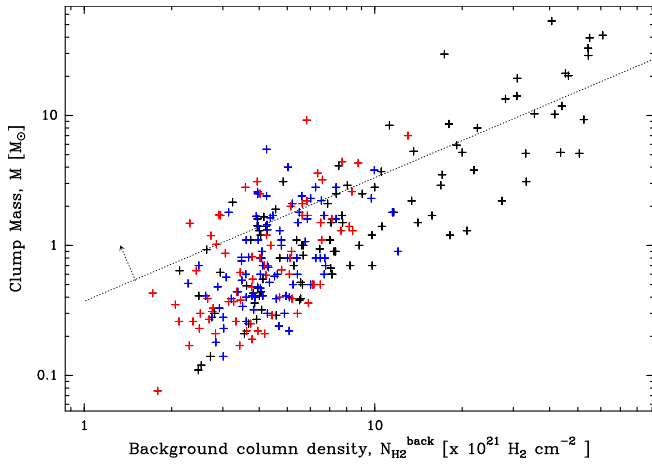

Fig. A5: A correlation is observed between the clump mass and its background column density. The color code highlighting the spatial location of the clumps is the same as in Fig. 7. The completeness curve in dotted line is calculated using a 90% completeness contrast of 1.1 and the M-N_{H2}^{peak} relation (see Figs. A2 and A3): $M = 0.34 \, (1.1 \times N_{H2}^{back})^{0.95}$